Draft version April 22, 2026
Typeset using LaTeX **twocolumn** style in AASTeX631

Mid-infrared JWST spectra of carbon stars in the Large Magellanic Cloud

G. C. Sloan,[1,2] B. Aringer,[3,4] Kathleen E. Kraemer,[5] J. Cami,[6,7] K. Eriksson,[3] S. Höfner,[3] K. Justtanont,[8] E. Lagadec,[9] Paola Marigo,[10,11] M. Matsuura,[12] I. McDonald,[13] E. J. Montiel,[14,15] R. Sahai,[16] and A. A. Zijlstra[13]

[1] *Space Telescope Science Institute, 3700 San Martin Drive, Baltimore, MD 21218, USA*
[2] *Department of Physics and Astronomy, University of North Carolina, Chapel Hill, NC 27599-3255, USA*
[3] *Theoretical Astrophysics, Department of Physics and Astronomy, Uppsala University, Box 516, 751 20 Uppsala, Sweden*
[4] *Department of Astrophysics, University of Vienna, Türkenschanzstraße 17, 1180 Wien, Austria*
[5] *Institute for Scientific Research, Boston College, 140 Commonwealth Avenue, Chestnut Hill, MA 02467, USA*
[6] *Department of Physics and Astronomy, The University of Western Ontario, London, ON N6A 3K7, Canada*
[7] *Institute for Earth and Space Exploration, The University of Western Ontario, London, ON N6A 3K7, Canada*
[8] *Chalmers University of Technology, Dept. Space, Earth and Environment, Onsala Space Observatory, 439 92 Onsala, Sweden*
[9] *Université Côte d'Azur, Observatoire de la Côte d'Azur, CNRS, Laboratoire Lagrange, Bd de l'Observatoire, CS 34229, 06304 Nice Cedex 4, France*
[10] *Department of Physics and Astronomy G. Galilei, University of Padova, Vicolo dell'Osservatorio 3, I-35122 Padova, Italy*
[11] *Deceased*
[12] *Cardiff Hub for Astrophysical Research and Technology (CHART), School of Physics and Astronomy, Cardiff University, The Parade, Cardiff CF24 3AA, UK*
[13] *Jodrell Bank Centre for Astrophysics, The University of Manchester, Manchester, M13 9PL, UK*
[14] *U.S. Naval Observatory, 3450 Massachusetts Ave. NW, Washington, DC 20392, USA*
[15] *SOFIA-USRA, NASA Ames Research Center, MS 232-12, Moffett Field, CA, 94035, USA*
[16] *Jet Propulsion Laboratory, MS 183-900, 4800 Oak Grove Dr., California Institute of Technology, Pasadena, CA 91109, USA*

ABSTRACT

Mid-infrared spectra from the Medium Resolution Spectrometer on the James Webb Space Telescope have revealed the molecular chemistry of carbon stars in the Large Magellanic Cloud with better resolution and sensitivity than previously possible. Our sample spans a range of dust-production rates and includes three relatively dust-free semiregular variables and six dustier Mira variables. All were observed 15–20 yr earlier with the Infrared Spectrograph on the Spitzer Space Telescope at lower spectral resolution. The new spectra show that the C_3 molecule is responsible for a strong absorption band centered at 5.2 μm. CS is clearly present in some of the sample, especially the stars with less dust. HCN also appears to be present. Some of the spectra have changed significantly between the Spitzer epoch and the MRS observations in 2023 and 2024, and in most cases these changes can be attributed to the stellar pulsation cycle. One exception is the disappearance of a dust emission feature at $\sim$18 μm in one of the Miras. The new spectra reveal a dip centered at $\sim$10 μm, which could arise either from an unknown carrier or from variable molecular emission to the red and blue. The presence of this spectral structure on the short-wavelength side of the SiC dust emission feature at $\sim$11.3 μm along with the broad C_2H_2 band centered at 14 μm raise the possibility that some previously reported detections of weak SiC dust emission in other carbon stars may not be real.

Keywords: carbon stars (199); asymptotic giant branch stars (2100); long period variable stars (935); circumstellar dust (236); circumstellar gas (238)

Corresponding author: G. C. Sloan gcsloan@stsci.edu

1. INTRODUCTION

Carbon stars dominate the population of evolved stars on the asymptotic giant branch (AGB) in the nearby Large and Small Magellanic Clouds (LMC and SMC; Blanco et al. 1978, 1980; Cioni & Habing 2003). They also dominate the production of dust in these metal-poor dwarf galaxies (Matsuura et al. 2009, 2013; Boyer et al. 2012; Srinivasan et al. 2016). AGB stars turn carbon-rich when they produce carbon via the triple-α process (Salpeter 1952) and dredge enough of it up to their surfaces to push the C/O ratio above 1.0 (e.g., Renzini & Voli 1981). These stars are unstable to pulsations in their envelopes, which trigger the mass loss that will strip them to their cores (e.g., Habing 1996; Mattsson et al. 2008; Liljegren et al. 2016; Höfner & Olofsson 2018).

Kraemer et al. (2019) showed that the amplitude of the pulsations is critical to the quantity and chemistry of the dust produced (see also McDonald & Trabucchi 2019). Carbon stars pulsating weakly as semiregular variables (SRVs) form small amounts of dust dominated by SiC. Carbon stars pulsating strongly enough to be classified as Mira variables produce significantly higher amounts of dust, primarily amorphous carbon, which dominates the dust as the stars evolve (Martin & Rogers 1987). Once a carbon star is forming amorphous carbon, the grains are opaque enough to be accelerated to escape velocity by radiation pressure from the central star and drag the gas along with it (e.g., Wickramasinghe et al. 1966; Woitke 2006; Mattsson et al. 2010; Bladh et al. 2019; Eriksson et al. 2023).

The dust condenses from molecular gas in the atmosphere, but a clear understanding of the molecular chemistry of that gas is lacking. Cherchneff et al. (2006) provides a good map of the reaction pathways and compounds to be expected. In a carbon-rich atmosphere, CO consumes all of the available oxygen, and molecules such as C_2H_2, HCN, SiS, and CS will form. All four have been identified in the mid-infrared spectra of Galactic carbon stars (Aoki et al. 1998, 1999), using the Short Wavelength Spectrometer (SWS; de Graauw et al. 1996; Leech et al. 2003) on board the Infrared Space Observatory (ISO; Kessler et al. 1996, 2003). Acetylene (C_2H_2) may be the primary building block of the benzene molecule (C_6H_6; Frenklach & Feigelson 1989), which in turn is the building block of graphite, amorphous carbon, and polycyclic aromatic hydrocarbons (PAHs; e.g., Allamandola et al. 1989).

The launch of the Spitzer Space Telescope (Werner et al. 2004) made it possible to obtain sizable mid-infrared spectroscopic samples of carbon stars in nearby galaxies in the Local Group, which enabled the study of how metallicity affects the photospheric chemistry and the production of dust in carbon stars. Using the Infrared Spectrograph (IRS) on Spitzer (Houck et al. 2004), several studies obtained spectra of a total of 144 carbon stars in the LMC (see Sloan et al. 2016, and references therein). The LMC has a metallicity that ranges between 30% and 50% Solar ($-0.5 <$ [Fe/H] < -0.3) (Piatti & Geisler 2013; Choudhury et al. 2016). Despite the difference in metallicity, carbon stars in the LMC and even the more metal-poor SMC show no notable differences in the quantity of dust produced compared to a sample of Galactic carbon stars observed by the SWS on ISO (Sloan et al. 2008). This trend continues to carbon stars in even more metal-poor dwarf spheroidal galaxies in the Local Group (Sloan et al. 2012). These results attest to the power of helium burning and dredge-ups on the AGB. Carbon stars are producing all the carbon they need to make dust themselves, no matter their initial metallicity. Thus, they are likely contributors to the dust in galaxies even in the high-redshift Universe (as discussed in Section 5.4).

While metallicity does not affect the dust-production rates in carbon stars strongly, the molecular component is another matter. In Galactic carbon stars, acetylene, HCN, CS, and SiS are all detected in the mid-infrared, but in the LMC and SMC, only acetylene has been observed (Aoki et al. 1998; Matsuura et al. 2006). This difference could arise from the lower metallicities of the stars, but the IRS spectra have a spectral resolving power ($R \equiv \lambda/\Delta\lambda$) of $\sim$100, which is high enough to study the molecular bands as a whole but too low to study the detailed structure within them. Thus, it is possible that low levels of absorption from molecules beside acetylene were present but went undetected.

This project follows up on carbon stars in the LMC previously observed with the IRS on Spitzer to better understand the nature of the molecular absorption in their spectra. We have observed a sample of carbon stars in the LMC with the Medium Resolution Spectrometer (MRS; Wells et al. 2015), an observing mode of the Mid-Infrared Instrument (MIRI; Wright et al. 2023) on board the James Webb Space Telescope (JWST; Gardner et al. 2023).

This paper presents an overview of the entire sample and focuses on (1) qualitative molecular analysis; (2) temporal spectral variations; and (3) their relation to the stellar pulsation cycles. Section 2 introduces the sample of spectroscopic targets; Section 3 describes the observations and data reduction; and Section 4 presents the results of the spectral analysis. Sections 5 and 6 discuss and summarize the results. The appendices exam-

ine the ancillary data used in this paper and supplement the figures from the spectral analysis.

2. SAMPLE

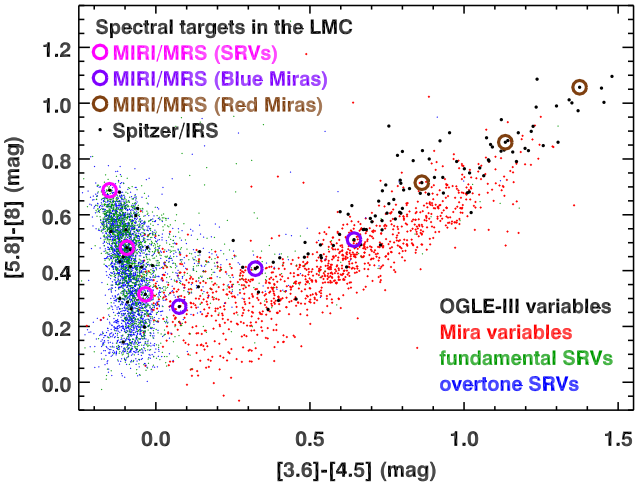

Figure 1. The sample of nine MRS targets (open circles) in color-color space defined by the four IRAC filters, plotted with data from the OGLE-III sample of carbon-rich long-period variables in the LMC (Soszyński et al. 2009) and the carbon stars observed by the IRS on Spitzer (Sloan et al. 2016). Three of the targets sample the SRV sequence (magenta), and the other six cover the Mira sequence (purple and brown).

JWST program 3010 observed nine carbon stars in the LMC with the MRS on MIRI in Cycle 2.[1] Table 1 provides details on the properties and observations of each star. Figure 1 plots the sample in infrared color-color space, along with all carbon-rich Mira variables and SRVs from the Optical Gravitational Lensing survey of the LMC (OGLE-III; Soszyński et al. 2009). The photometry comes from the Infrared Array Camera (IRAC) on Spitzer (Fazio et al. 2004), the Wide-field Infrared Survey Explorer (WISE; Wright et al. 2010), and the Near-Earth Object WISE Reactivated mission (NEOWISE-R; Mainzer et al. 2014). The data in the 3.4 and 4.6 μm WISE filters (W1 and W2) have been shifted to the IRAC 3.6 and 4.5 μm filters using the conversions from Sloan et al. (2016).

The colors of the carbon stars follow two distinct sequences. The Mira variables, which are undergoing strong fundamental-mode pulsations in their atmospheres, lie to the right of the boundary at [3.6]−[4.5] ∼ 0. The SRVs lie to the left of that boundary, no matter their pulsation mode. Sloan et al. (2015) suggested that the range of [5.8]−[8] colors in the SRVs could arise from differing levels of absorption from C_3 at 5 μm, based on the identification of C_3 in SWS spectra of Galactic carbon stars (Loidl et al. 1997; Gautschy-Loidl et al. 2004). Deeper C_3 absorption would decrease the emission in the 5.8 μm filter and redden the [5.8]−[8] color. See Sec. 4.2.3 for new observational support of this hypothesis. In the Mira variables, on the other hand, the increasing red colors in all filters result from higher optical depths of amorphous carbon dust around them.

We selected nine targets in Program 3010 to track both the SRV and Mira sequences in Figure 1, with three stars along the SRV sequence and six along the Mira sequence. We chose targets that had been previously observed by the IRS on Spitzer, were roughly evenly spaced along the two sequences, and were close to the bar of the LMC so that they were observed in six epochs with IRAC on Spitzer. The first two IRAC epochs were from the program Surveying the Agents of a Galaxy's Evolution (SAGE), which surveyed the entire LMC (Meixner et al. 2006). The other four epochs were obtained in the SAGE-Var program (Riebel et al. 2015).

Figure 1 shows the Spitzer/IRS sample of carbon stars in the LMC as black dots. The nine sources also observed by the MRS on JWST are circled in magenta (for the SRVs) and purple and brown (for the bluer and redder Miras, respectively).

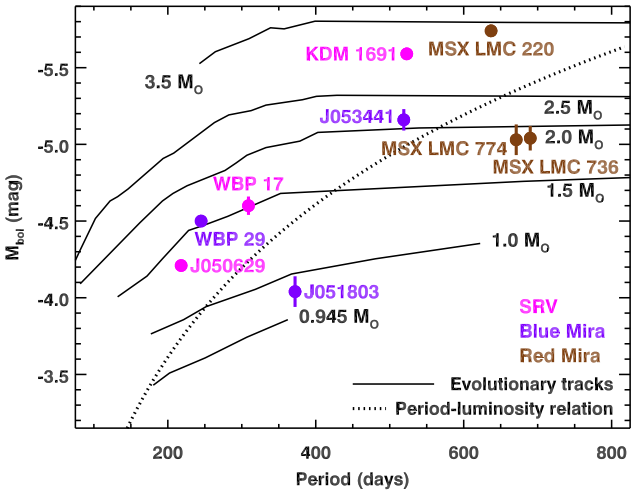

Figure 2. The stars in our sample compared to evolutionary tracks by Vassiliadis & Wood (1993) and the period-luminosity relation for carbon stars (Whitelock et al. 2009). Appendix B describes how the luminosities were calculated.

[1] DOI: 10.17909/j0jj-1h55

Table 1. The MRS Sample of Carbon Stars in the LMC

Target[a]	R.A.	Decl.	Var. Type	Period	Luminosity	[3.6]−[4.5]	Integration Time	IRS Epoch	MRS Epoch
	(J2000)			(days)[b]	($L_\odot$)[c]	(mag)[d]	(s)	(MJD)	(MJD)
J050629	76.623347	−68.926346	SRV	(218)	3820 ± 3	−0.150	5784	54484	60273
KDM 1691	75.903917	−68.560699	SRV	523	13,650 ± 560	−0.094	1340	54649	60551
WBP 17	81.582833	−69.693703	SRV	309	5510 ± 310	−0.034	4224	53596	60551
WBP 29	81.670642	−69.386490	Mira	245	5010 ± 50	0.076	5112	53482	60274
J051803	79.513592	−68.830750	Mira	372	3270 ± 300	0.323	1560	54688	60490
J053441	83.672587	−69.441864	Mira	519	9190 ± 590	0.643	540	54611	60551
MSX LMC 220	78.133621	−69.261230	Mira	637	15,760 ± 530	0.863	540	53379	60551
MSX LMC 774	81.596238	−69.188965	Mira	671	8180 ± 720	1.134	540	53445	60551
MSX LMC 736	83.278350	−70.509682	Mira	690	8210 ± 620	1.375	628	54611	60385

[a] The three stars with names beginning with "J" have the more formal coordinate-based names 2MASS J0506290−6855348, SSTISAGE1C J051803.23−684950.7, and 2MASS J05344142−6926307. This paper will refer to them by their shorter "J" names throughout.

[b] See Appendix A. Values in parentheses are uncertain.

[c] See Appendix B.

[d] From photometry reported by Sloan et al. (2016).

Table 1 provides the pulsation periods and luminosities of the stars in the sample, which were determined as described in Appendices A and B, respectively. Figure 2 compares the properties of the sample to evolutionary tracks from Vassiliadis & Wood (1993), which give a rough idea of the initial mass of the stars. KDM 1691 and MSX LMC 220 are significantly more luminous than the rest of the sample and thus more massive and in all likelihood more metal-rich. J051803 appears to be the least massive and therefore oldest and most metal-poor star in the sample. The SRVs are all to the left of the period-luminosity relation determined by Whitelock et al. (2009), which is arguably consistent with overtone pulsation modes, but the spread in the Miras to either side of the relation indicates that the relation must be broad and not well defined by a single curve.

3. OBSERVATIONS AND DATA REDUCTION

Each of the nine stars in the sample was observed in all three grating settings in the MRS, giving complete coverage at a spectral resolving power of ∼2000–3000 from 4.9 to 28 μm. The combination of decreasing emission from the stars and lower sensitivity in Channel 4 of the MRS (18–28 μm make the spectra less meaningful past a limit of ∼19–22 μm, depending on the brightness of the star. Integration times were set to achieve a minimum signal-to-noise ratio (S/N) of ∼100 from 5 to 12 μm. For the reddest three stars in the sample, the S/N stayed above ∼100 out to ∼18 μm. Each target was observed with the four-point dither pattern optimized for point sources in all MRS channels.

The spectral data were processed using the JWST pipeline version 1.18.0 and Calibration Data Reference System (CRDS) context jwst_1364.pmap. This version of the pipeline processed the 12 spectral segments (four channels, three grating segments) separately and applied the optional residual defringing algorithm to each. The extraction of the spectra used the default pipeline sequence that first combines the four dither positions to construct a resampled spatial/spectral data cube for each spectral segment. The pipeline then extracts spectra from the data cubes using a circular aperture and background annulus with radii that increase linearly with wavelength. The MRS data cubes showed that our targets dominated their immediate environment. The flux calibration produces results within 1% of the IRS on Spitzer for standard stars observed by both (Law et al. 2024). Figures 3 to 5 present the resulting spectra from the MRS and compare them to the IRS.

4. SPECTRAL ANALYSIS

4.1. *The Manchester Method*

We have measured the strength of the acetylene absorption band at 7.5 μm and the SiC dust feature at

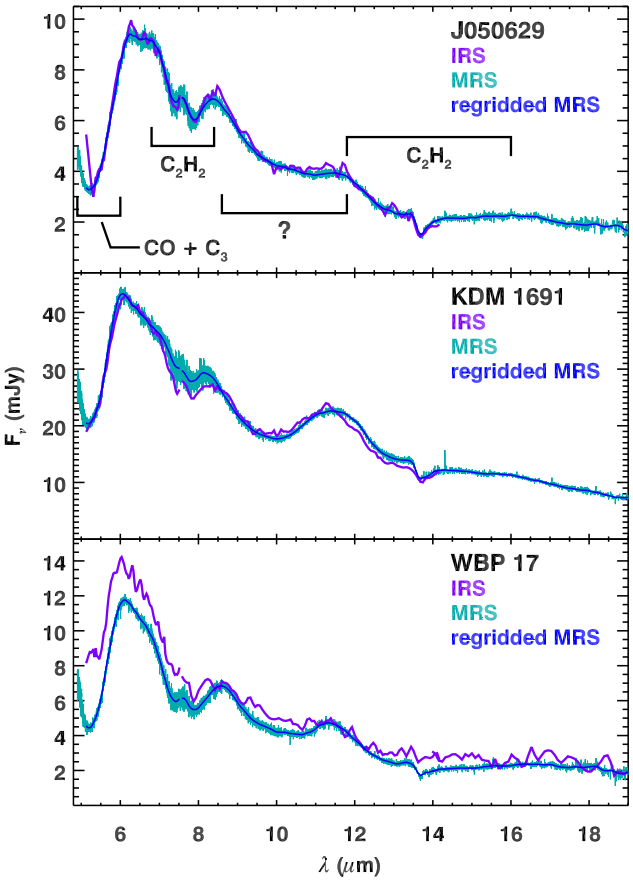

Figure 3. MRS spectra of the three SRVs, compared to the spectra from the IRS. The spectra from the MRS are plotted as produced by the pipeline and also after regridding them to the lower-resolution wavelength grid of the IRS.

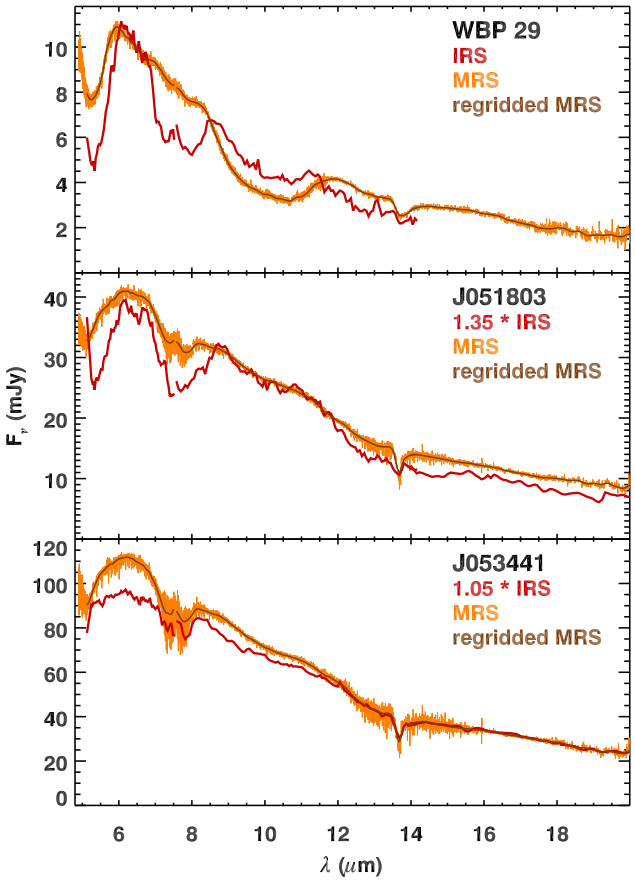

Figure 4. MRS spectra of the three bluest of the six Mira variables, compared to the spectra from the IRS. As in Figure 3, the spectra from the MRS are plotted before and after regridding to the IRS. Two of the IRS spectra have been scaled up multiplicatively, to match the brightness of the MRS spectra, to make comparisons easier.

~11.5 μm using the Manchester Method, which estimates the continuum by fitting a line segment to either side of the spectral features. Sloan et al. (2016) describe this method and its history (see their Figures 1–2 for illustrations). While the Manchester Method is arguably simplistic, it does provide a quick measurement using a method applied to hundreds of other carbon-star spectra for comparison. It also provides a color in two discrete wavelength bands centered at 6.4 and 9.3 μm, which sample spectral regions that come closer to continuum than most others in these complex spectra. The "continuum" in these spectra is a combination of emission from the star and amorphous carbon dust, which has no resonances and thus no spectral features in the infrared. The [6.4]−[9.3] color measures the amount of amorphous carbon dust around the star, with higher dust-production rates leading to increasingly red colors (Groenewegen et al. 2007).

Table 2 gives the results for the [6.4]−[9.3] color, the equivalent width of the acetylene absorption at 7.5 μm, and the strength of the SiC dust emission feature at ~11.3 μm with respect to the continuum. Figures 6 and 7 plot the strengths of the acetylene absorption and SiC emission versus the [6.4]−[9.3]. Both figures exclude the eight deeply reddened carbon stars observed with the IRS in the LMC with [6.4]−[9.3] > 2.0.

For the absorption band and the dust emission, Table 2 reports a central wavelength, defined as the wavelength that bisects the absorption or emission. It provides a useful check of the extracted feature. All of the acetylene bands have central wavelengths between 7.45 and 7.68 μm and appear to be valid, even the weak band in WBP 29. For SiC dust emission, the central wavelength of the extracted feature calls into question the presence of SiC in three spectra. The sample of carbon stars in the LMC compiled by Sloan et al. (2016) includes 123 sources with an SiC/continuum ratio > 0.05

Table 2. Spectroscopic Data

Target	[6.4]−[9.3]	C_2H_2 at 7.5 μm		SiC Dust Emission	
		Wavelength[a]	Eq. width[b]	Wavelength[a]	SiC/Continuum[bc]
	(mag)	(μm)	(μm)	(μm)	
J050629	0.144 ± 0.003	7.673 ± 0.010	0.155 ± 0.001	11.547 ± 0.011	(0.097 ± 0.001)
KDM 1691	0.031 ± 0.002	7.513 ± 0.008	0.102 ± 0.001	11.381 ± 0.006	0.238 ± 0.001
WBP 17	−0.001 ± 0.004	7.460 ± 0.004	0.335 ± 0.001	11.420 ± 0.009	0.180 ± 0.001
WBP 29	−0.130 ± 0.003	7.411 ± 0.023	0.012 ± 0.001	12.165 ± 0.033	(0.023 ± 0.002)
J051803	0.452 ± 0.001	7.476 ± 0.005	0.106 ± 0.001	11.079 ± 0.018	(0.038 ± 0.001)
J053441	0.452 ± 0.001	7.454 ± 0.003	0.122 ± 0.001	11.266 ± 0.021	0.045 ± 0.001
MSX LMC 220	0.830 ± 0.001	7.538 ± 0.016	0.039 ± 0.001	11.329 ± 0.013	0.090 ± 0.001
MSX LMC 774	0.908 ± 0.001	7.480 ± 0.004	0.107 ± 0.001	11.292 ± 0.008	0.141 ± 0.001
MSX LMC 736	1.147 ± 0.001	7.556 ± 0.008	0.133 ± 0.001	11.325 ± 0.009	0.155 ± 0.001

[a] The central wavelength of the band or feature as defined in the text.

[b] Uncertainties are lower limits; they do not account for systematic effects, as Section 4.1 explains.

[c] Questionable measurements are in parentheses, as explained in Section 4.1.

(out of 184). For those, the mean central wavelength = 11.293 ± 0.113. Letting two standard deviations define the range of valid central wavelengths gives a range of 11.07–11.52 μm. Both WBP 29 and J050629 are outside this range, leading to doubts that their spectra contain SiC dust. In one other source, J051803, the emission feature is close to the blue edge, faint, and therefore also questionable.

The uncertainties in the strengths of the extracted features in Table 2 are statistical. They should be treated as lower limits, because they do not include the systematic effects resulting from how spectral structure (from molecular bands or solid-state features) on either side of the band or feature considered might affect the continuum. In the case of the SiC dust emission feature, absorption from C_2H_2 to the red will affect the fitted continuum and thus the measured strength. As discussed in Section 5.2, molecular absorption may also affect the fitted continuum on the blue side of the SiC dust. Thus, a high ratio of feature strength to uncertainty does not necessarily mean the feature is real.

4.2. *Analysis of the detailed molecular band structure*

The analysis uses a grid of synthetic spectra based on hydrostatic models with effective temperatures of 3100 and 2800 K, a range of C/O ratios from 1.05 to 4.0, M = 1.0 $M_\odot$, log g (cm s^{-2}) = 0.0, and a metallicity ([Z/H]) of −0.5. The models are based on the COMARCS code (Aringer et al. 2016, 2019). The models use EXOMOL line lists for C_2H_2 (Chubb et al. 2020), C_3 (Lynas-Gray et al. 2024), HCN (Harris et al. 2008; Barber et al. 2014), and CS (Paulose et al. 2015), and the HITEMP line list for CO (Li et al. 2015)[2]. The models include isotopologs of the above molecules (at solar abundances), other molecules, and atomic transitions.

The hydrostatic models provide synthetic spectra with detailed band structure for individual molecules, which can greatly aid the identification of what is absorbing in different wavelength regions. The hydrostatic models do not include pulsation, convective structures, or winds, and as a consequence they will not include the cooler layers of gas likely to be responsible for much of the observed molecular spectral structure. As a result, we should not expect the band depths or relative strengths of the available transitions in the synthetic spectra to match the observed spectra. The present analysis focuses on the detailed spectral structure within short wavelength intervals rather than attempting to model the overall band strength and shape. With the exception of measuring radial velocities, the analysis is more qualitative than quantitative.

We confine the spectral analysis in this work to what can be called the "flatten-and-fit" method. We have broken the spectra into multiple wavelength intervals, with intervals at 4.9–5.2 and 5.2–5.5 μm to investigate the absorption by CO and C_3, 7.0–7.5, 7.5–8.0, and 8.1–

[2] https://hitran.org/hitemp

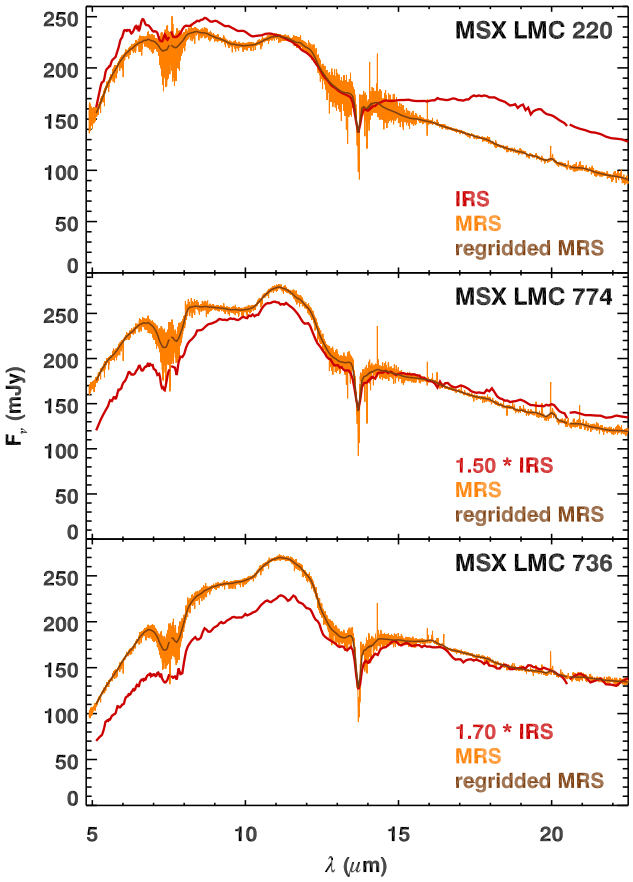

Figure 5. MRS spectra of the three reddest Mira variables, compared to the spectra from the IRS. As in Figure 4, the MRS spectra are plotted before and after regridding, and two of the IRS spectra have been shifted up multiplicatively, to align with the MRS.

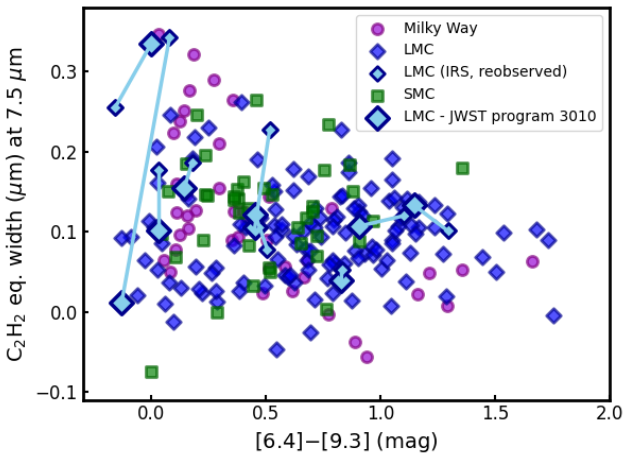

Figure 6. The equivalent width of the 7.5 μm acetylene absorption band as a function of the [6.4]−[9.3] color. The nine stars in the present sample are plotted as small light-blue diamonds, as observed by the IRS, and large light-blue diamonds, as observed by the MRS. WBP 29 has moved dramatically from top left to bottom left, due to its disappearing acetylene band. Section 5.1 discusses the temporal changes at 7.5 μm in WBP 29 and the other sources.

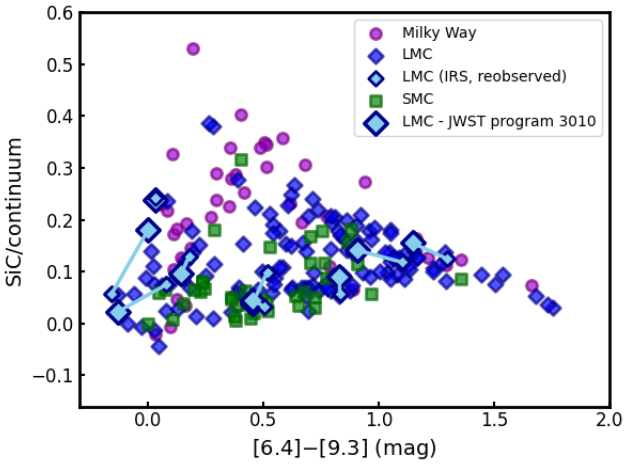

Figure 7. The strength of the SiC dust emission feature versus the [6.4]−[9.3] color, with IRS and MRS results plotted as in Figure 6.

8.6 μm for C_2H_2, HCN, and CS, and 12.6–13.1, 13.1–13.6, and 13.8–14.3 μm for C_2H_2 and HCN.

In each interval, we take the following steps: (1) create a pseudo-continuum from the observed spectrum, by generating a median with a 100-pixel interval; (2) divide the spectrum by that pseudo-continuum to isolate the spectral structure within the band; and (3) subtract 1.0 so that the spectral emission and absorption structure oscillates around a mean value of 0.0. The pseudo-continuum runs through the middle of the band structure and not the top, as might be more appropriate for an absorption spectrum. The synthetic molecular absorption spectra follow the same steps, except that we initially downsampled them to the wavelength grid and resolution of the MRS, using the resolutions as defined by Pontoppidan et al. (2024). When fitting the synthetic absorption to an observed spectrum, we normalize the synthetic spectrum to the mean of the absolute value of the observed spectrum across a wavelength interval. The acetylene band at 7.5 μm flattens pretty well, but the deep and narrow Q branch from the ν_5 band at 13.7 μm retains some of its structure, which is why the chosen intervals skip from 13.6 to 13.8 μm. We placed the 8 μm interval at 8.1–8.6 μm, to concentrate on the region where CS absorbs most strongly.

4.2.1. *Radial velocities*

To determine the radial velocities of the stars in the sample, we used the synthetic spectra from hydrostatic

Table 3. Radial Velocities

Target	$T_{\rm eff}$	Radial Velocity in Wavelength Interval[a] (km s^{-1})								Mean Radial Velocity[b]
	(K)	4.9–5.2 μm	5.2–5.5 μm	7.0–7.5 μm	7.5–8.0 μm	8.1–8.6 μm	12.6–13.1 μm	13.1–13.6 μm	13.8–14.3 μm	(km s^{-1})
J050629	3100	244	(184)	229	250	240	(180)	248	(263)	242 ± 4
KDM 1691	3100	278	270	260	266	261	239	277	(183)	264 ± 5
WBP 17	3100	289	270	261	267	261	238	277	266	266 ± 5
WBP 29	2800	240	229	224	240	(238)	(180)	228	247	235 ± 4
J051803	2800	241	179	224	204	(271)	(180)	223	(235)	214 ± 11
J053441	2800	244	(226)	224	204	(275)	(180)	223	(228)	224 ± 8
MSX LMC 220	2800	240	184	213	203	240	(178)	206	(183)	214 ± 9
MSX LMC 774	2800	241	221	234	227	(276)	(180)	221	(183)	229 ± 4
MSX LMC 736	2800	277	226	224	206	(278)	189	258	(316)	230 ± 13

[a] Velocities in parentheses were not used.

[b] Uncertainties are the uncertainties in the mean.

models and the flatten-and-fit method described in Section 4.2. Table 3 gives the resulting radial velocities for each star in each wavelength interval, as well as the mean. For the SRVs, we used the synthetic spectra from models with an effective temperature $T_{\rm eff}$ = 3100 K, and for the Miras, with 2800 K. For all stars, we used synthetic spectra from models with a C/O ratio = 2.0. Each wavelength interval was fitted separately, by iterating in 1 km/s steps from 160 to 320 km/s and also through different mixtures of the two to three molecules contributing to each interval. Generally, the best radial velocity depended only weakly on the details of the chemical mixture.

This procedure comes with a number of caveats. First, the flatten-and-fit method does not fit the depth of a full absorption band; it just fits the fine-scale spectral structure in that band or combination of bands. The only molecules we considered were CO, C_3, C_2H_2, HCN, and CS (and not their isotopologs). Other molecules are certainly contributing to the spectra. As already noted, the spectra show evidence of absorption from molecules much cooler than one might expect in a hydrostatic model, and that difference in temperature could shift the relative line strengths within unresolved band structure and thus the apparent radial velocity. We broke broader spectral regions into smaller wavelength intervals to reduce the effect of an incorrect temperature over larger wavelength ranges. Finally, the line lists may have errors in the predicted line positions and intensities, and they may not be complete, which will increase the residuals in the fitting process.

All of the limitations just described mean that the systematic differences between the observed and synthetic spectra dominate the noise in the data, which results in a high floor to the χ^2 residuals. That prevents us from estimating the uncertainty in a radial velocity fitted to an individual spectral segment. Instead, we have estimated the uncertainty in the mean radial velocity for each star, based on the standard deviations of the radial velocities from the separate spectral segments (up to eight). These velocities can vary significantly between intervals for a given star, due in part to the caveats already described. It is also possible that some of the differences are real, as different molecules could be tracing different layers in the pulsating stellar atmosphere. Even for the same molecule, absorption at different wavelengths could arise from gas at different opacities and thus different temperatures and layers. Nonetheless, we are able to determine radial velocities with uncertainties of less than 10 km/s in most cases.

Table 3 presents several radial velocities in parentheses, because the fitting method did not produce a satisfactory minimum. In the 8.1–8.6 μm interval, five of the six Mira variables did not show well-defined minima in their χ^2 residuals. The 12.6–13.1 and 13.8–14.3 μm intervals were also difficult, leading us to use the fitted radial velocities in only the best-behaved cases. We rejected two of the fitted velocities at 5.2–5.5 μm for the same reason.

Our radial velocities compare well to those from Gaia DR3 (Gaia Collaboration 2016, 2023). Gaia has radial velocities for three stars in our sample. For KDM 1691, Gaia gives $v_{\rm rad} = 260 \pm 1$ km/s, compared to the MRS result of 264 ± 5 km/s. For WBP 17, $v_{\rm rad} = 261 \pm 6$ from Gaia and 266 ± 5 from the MRS, and for WBP 29, the corresponding results are $v_{\rm rad} = 240 \pm 3$ and 235 ± 4. In all three cases, the error bars overlap.

4.2.2. *General results*

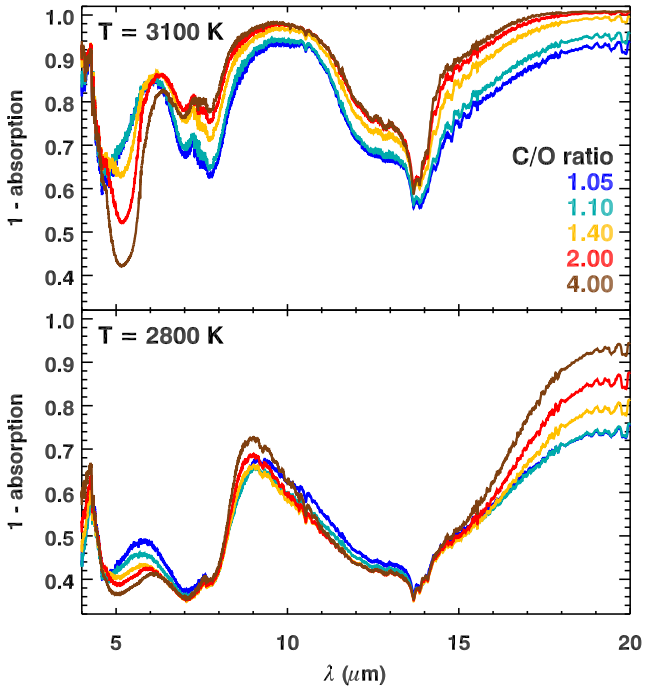

Figure 8. The absorption in the synthetic spectra based on hydrostatic models at two temperatures and five C/O ratios. The models have been regridded to the MRS wavelength grid and then smoothed with a 29 pixel boxcar. The 2800 K models show that the spectra are never even close to a real continuum in the mid-infrared.

Figure 8 plots synthetic spectra from the hydrostatic models at $T_{\rm eff} = 2800$ and 3100 K at five different C/O ratios. The synthetic spectra are normalized relative to a continuum taken from a calculation without any line opacities. The most important takeaway is in the 2800 K models, where the absorption is substantial throughout the mid-infrared. The spectra are nowhere near a true continuum level anywhere between 5 and 17 μm. That behavior illustrates how the Manchester Method is making broad assumptions about what can be used for a local "continuum."

In most cases in Figure 8, the acetylene absorption band at 7.5 μm in the synthetic spectra does not have the classic "W" shape seen in the observed spectra. A comparison of the observed and 3100 K synthetic spectra in the top and middle panels of Figure 9 shows the difference more clearly. In the hydrostatic models, the C_2H_2 absorption occurs in a layer with a temperature of ∼1200–1500 K, but to reproduce the "W" shape, the absorbing gas needs to be below 1000 K. Matsuura et al. (2006) were able to reproduce the band shape with a slab of absorbing C_2H_2 at 500 K. They also noted that the observed C_2H_2 absorption at 13.7 μm in carbon stars heavily obscured by circumstellar dust requires that the absorbing gas be above the dust photosphere, which would be in the circumstellar envelope and well above the stellar photosphere. Hydrostatic models do not reproduce this structure, which is why the present analysis is limited to the flattening-and-fitting method.

Table 4 presents the results of our analysis of the flattened spectra, where we have fitted the relative molecular contributions in the smaller wavelength intervals listed in Table 3 and combined the results into groups of wavelength intervals. Where a molecule clearly dominates the absorption, it is in bold type. Otherwise, the order of the molecules listed is not significant. Analysis based on more realistic models would be required for quantitatively meaningful relative abundances. Appendix C plots the best-fitting models in each wavelength interval for each star.

4.2.3. *C_3 and CO at 5 μm*

Figure 9 compares the observed spectra of the SRVs with synthetic spectra based on 3100 K models after the spectra have been smoothed with a 29 pixel boxcar. The spectra of the SRVs all show a minimum at ∼5.2 μm, matching the shape of the C_3 band in the synthetic spectra. The CO band, on the other hand, has a bandhead further to the blue at ∼4.6 μm. The synthetic spectra show that the C_3 band increases in strength as the C/O ratio increases, and it also grows wider. As in Figure 8, the absorptions in the synthetic spectra are based on ratios to synthetic spectra of models computed without line opacities.

Figure 10 compares the detailed band structure in the SRVs to absorption from C_3 and CO in synthetic spectra based on hydrostatic models with $T_{\rm eff} = 3100$ K and C/O = 2.0. While the measured χ^2 residuals are smaller for the SRVs when using C_3 instead of CO, the residual spectra in Figure 10 show only a subtle improvement. This discrepancy between the apparent match at low resolution in Figure 9 and the higher resolution could arise from the limitations of the synthetic spectra used in this analysis. If the model does not reproduce

Table 4. Identified Molecules

Target	Identified Molecules in Wavelength Range[a]			
	5 μm	7–8 μm	8.1–8.6 μm	13–14 μm
J050629	**C_3**, CO	**C_2H_2**, HCN, CS	**CS**, C_2H_2	**C_2H_2**, HCN
KDM 1691	**C_3**, CO	C_2H_2, HCN, CS	**CS**	**C_2H_2**, HCN
WBP 17	**C_3**, CO	C_2H_2, HCN, CS	**CS**, HCN	**C_2H_2**, HCN
WBP 29	**C_3**, CO	C_2H_2, HCN, CS	**HCN**	**C_2H_2**, HCN
J051803	**C_3**, CO	**C_2H_2**, HCN, CS	**CS**	**C_2H_2**, HCN
J053441	**C_3**, CO	**C_2H_2**, HCN, CS	**CS**	**C_2H_2**, HCN
MSX LMC 220	**C_3**, CO	**C_2H_2**, HCN, CS	HCN, CS	**C_2H_2**, HCN
MSX LMC 774	**C_3**, CO	**C_2H_2**, HCN, CS	**CS**, HCN	**C_2H_2**, HCN
MSX LMC 736	**CO**, C_3	**C_2H_2**, HCN, CS	**CS**, HCN	**C_2H_2**, HCN

[a]Dominant molecules are in **bold**. Otherwise, the order is not significant.

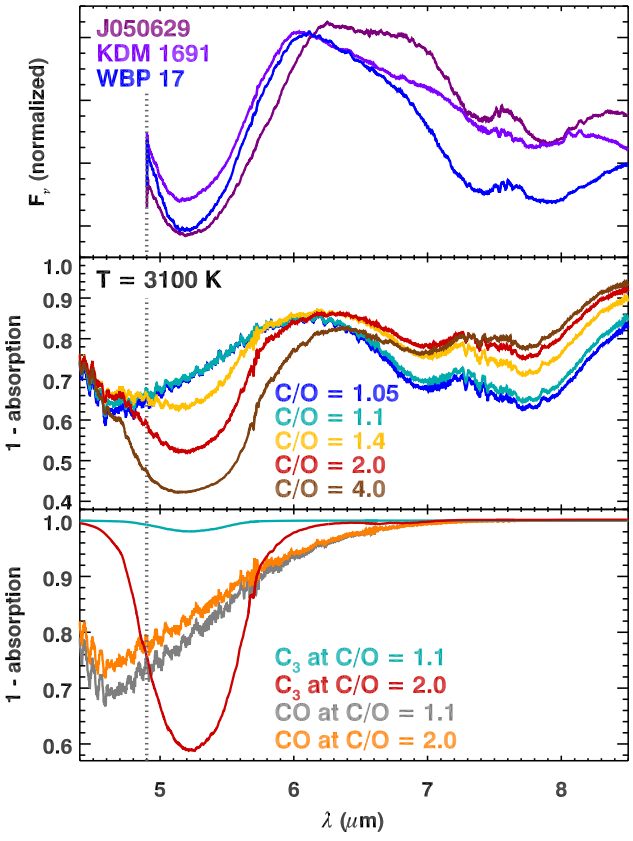

Figure 9. Observed spectra of the SRVs compared to absorption in the synthetic spectra from 4.4 to 8.5 μm at low spectral resolution. The MRS spectra and synthetic spectra have been smoothed with a 29 pixel boxcar. The vertical dotted line at 4.9 μm marks the blue edge of the MRS data. *Top:* observed MRS data. *Middle:* full absorption of all molecules and atoms considered in the models at $T_{\rm eff}$ = 3100 K. *Bottom:* absorption from C_3 and CO.

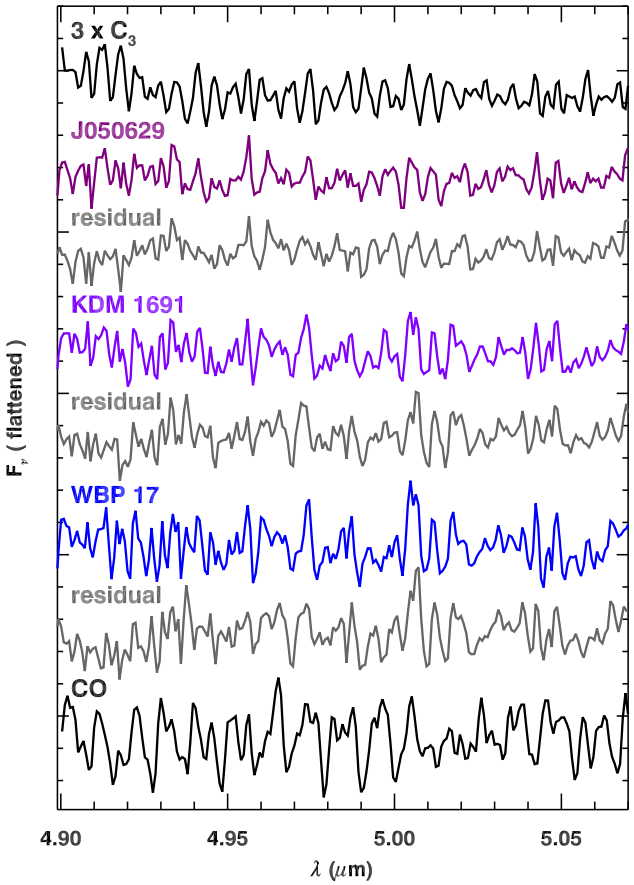

Figure 10. A comparison of the band structure of C_3 and CO to the flattened spectra of the SRVs between 4.9 and 5.07 μm. The synthetic spectra (black, top and bottom) are for $T_{\rm eff}$ = 3100 K and C/O = 2.0. Residual spectra after fitting and removing C_3 are plotted in gray below the spectra for the three sources.

the actual pressure and temperature of the absorbing

gas, then the relative strengths of the individual transitions within the bands could differ, which would limit our ability to fit the band structure in detail. Other molecules not considered in our analysis may also contribute to the spectral structure. Nonetheless, based on the similarity of the shape of the observed and synthetic absorption band at 5.2 μm at low resolution, we conclude that C_3 is the likely carrier of the observed band in the SRVs. That conclusion results primarily from the improved wavelength coverage of the MRS, down to 4.9 μm, compared to 5.1 μm with the IRS on Spitzer, which shows that the spectra turn up at ∼5 μm, as expected for C_3.

The low-resolution spectra from the IRS typically cease to be meaningful below 5.1 μm, while the MRS data are good to 4.9 μm. The additional 0.2 μm greatly helps our ability to identify C_3, as the upturn below the wavelength of peak absorption (5.2 μm) is unambiguous. Figures 3–5 show that C_3 is clearly present in the three SRVs and the three blue Miras, but not as obvious in the three red Miras.

Comparing the spectra from the MRS to the synthetic spectra supports the hypothesis that C_3 explains the range of reddening in the [5.8]−[8] color in the SRVs, which can be seen in Figure 1. The synthetic spectra suggest further that the cause of the varying quantities of C_3 may be the C/O ratio in the atmosphere of the SRV. However, this conclusion is only qualitative, due to the limits of the hydrostatic models. The actual C/O values needed to reproduce the depth and shape of the observed C_3 band require further investigation.

4.2.4. *CS at 8 μm*

Figure 11 compares the 8.1–8.6 μm spectra of the three SRVs with CS from the synthetic spectrum from a 3100 K model with C/O = 2.0. Including CS reduces the residuals in all three spectra, and the improvement is particularly clear in KDM 1691 and WBP 17. The other possible contributors—C_2H_2 and HCN—have different spectral signatures in this wavelength interval, as can be seen in the spectra in Appendix C. The spectra in Appendix C reveal that CS is present in the SRVs in the 7.5–8.0 μm interval, too. Thus, the MRS and its higher spectral resolution can detect CS, while the lower resolution of the IRS on Spitzer ($R \sim 100$) could not (Matsuura et al. 2006).

4.2.5. *HCN*

Matsuura et al. (2006) did find evidence of HCN in one or two Magellanic carbon stars in their low-resolution IRS spectra. The spectra from the MRS present stronger evidence, but no clear proof like that found for CS. The iterative fitting process of the flattened spectra found for all nine stars in the sample that the presence of HCN results in lower χ^2 residuals in most or all of the wavelength intervals from 7.0 to 14.3 μm. The figures in Appendix C compare the observed spectra with HCN and other possible contributors. Thus, while the evidence for HCN is not conclusive, it is strong.

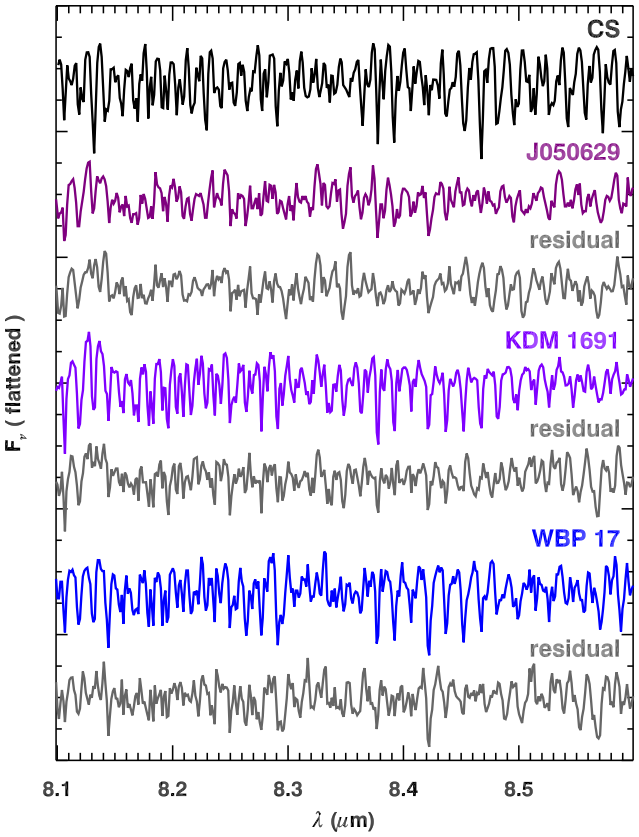

Figure 11. The 8.1–8.6 μm spectra of the three SRVs (in color), the synthetic spectrum of CS from the hydrostatic model at 3100 K and C/O = 2.0 (black), and residual spectra after fitting and removing CS (gray). CS is clearly present in KDM 1691 and WBP 17, and while less visible in J050629, is required to minimize the residuals.

5. DISCUSSION

5.1. *WBP 29 and spectral variations in the sample*

While WBP 29 is classified as a Mira variable, it lies close in color-color space to the boundary with the SRVs (Figure 1). Its pulsational properties separate it from the other Miras. It has the shortest pulsational period of the Miras, and, for the Miras where we have measured the pulsation amplitudes with confidence, it has the lowest amplitude (Table 6 in Appendix A).

WBP 29 may be in transition from an SRV to a Mira, and its spectrum has changed dramatically between the IRS epoch (approaching minimum) and the MRS epoch

(near maximum). Between those epochs, the 7.5 μm acetylene band almost disappeared, and an apparent 10 μm absorption band emerged in its place (Figure 4). Sloan et al. (2024) raised the possibility that the changes in its spectral properties could arise from evolutionary changes in the star itself, as opposed to changes one might expect over the pulsation cycle of the star.

Since then, we have investigated the infrared light curve of WBP 29 more thoroughly (Appendix A), and we have also investigated the question of the apparent 10 μm absorption band in archival data from the SWS on ISO (Appendix D). The SWS data reveal that the 10 μm band can be seen in the spectra of four Galactic carbon stars observed in multiple epochs, and that it generally is strongest when the star is at maximum in its pulsation cycle, which is also the case for WBP 29. The relation of the 10 μm absorption to stellar pulsation rules out an interstellar origin; it must be circumstellar.

With the completion of the observations of the rest of the sample, we can place WBP 29 in better context. To examine the behavior of the 7.5 μm absorption, we can compare the shift in positions in Figure 6 with the positions of the IRS and MRS epochs on the light curves in Appendix A. We exclude J050629 from consideration, due to insufficient phase information. KDM 1691 was observed by the IRS at minimum and by the MRS at maximum, and its 7.5 μm band has weakened. J053441 was observed near minimum by the IRS and near maximum by the MRS, and the 7.5 μm band has weakened in its spectrum also. WBP 17 was observed at maximum by the IRS and at minimum by the MRS, and, once again, the observation at minimum has the stronger absorption at 7.5 μm.

In J051803, on the other hand, the 7.5 μm band has grown slightly stronger in the MRS observation, which was closer to maximum, compared to the IRS observation, which was halfway from minimum to maximum. That suggests that the behavior of the 7.5 μm depends on more than just pulsation phase. Similarly, the three reddest Miras present a mixed bag. All three were observed at or near minimum by the IRS and by the MRS at or near maximum. However, the changes in the 7.5 μm band strength are not large, and only two of the three stars (MSX LMC 220 and 774) follow the trend of stronger absorption at minimum. It is possible in these three redder stars that the absorbing layer is much higher above the photosphere and does not vary as strongly with the pulsations in the star below it.

To summarize, WBP 29 appears to follow the weak trends of weaker 7.5 μm absorption and stronger apparent 10 μm absorption close to maximum in its pulsation cycle. We conclude that the observed spectral variations most likely result from its pulsations, as opposed to evolutionary changes.

5.2. *The impact of the apparent 10 μm absorption band*

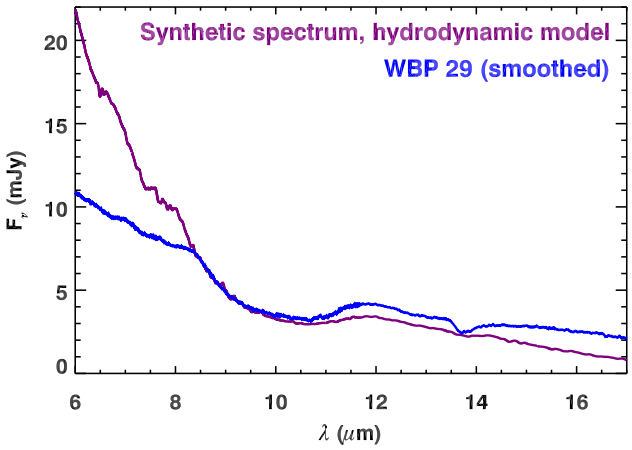

Figure 12. The synthetic spectrum of a hydrodynamic model of a carbon star, computed without dust opacities and scaled to the spectrum of WBP 29. The synthetic spectrum has been downsampled to the MRS wavelength grid and resolution, and the observed spectrum has been smoothed with a 15 pixel boxcar. The model is representative and not fitted specifically to WBP 29. It is for a 1 $M_\odot$ star with $T_{\rm eff}$ = 3000 K and L = 7000 $L_\odot$.

The spectra of the SRVs and the blue Mira WBP 29 in Figures 3 and 4 show a clear depression centered at 10 μm, which could be a molecular absorption band. The depth of this feature and the position of its long-wavelength edge may vary between objects and with time. As Appendix D shows, some Galactic carbon stars observed by the SWS behave similarly.

The carrier of the apparent absorption band at 10 μm is uncertain. We were unable to match the spectral structure in that region closely to any of the molecules considered in the synthetic spectra based on hydrostatic models (viz C_2H_2, HCN, CS, CO, and C_3). An unidentified molecule not included in our models could be responsible.

Another possibility is that the apparent absorption at 10 μm arises from molecular emission to either side, at 7.5 and 12–15 μm, most likely from C_2H_2, with possible contributions from HCN. These molecules have millions of overlapping transitions in this spectral region, which could produce a raised quasi-continuum in the right conditions. Those conditions could be met if the pulsations in the carbon stars are strong enough to push a layer of gas high above the stellar photosphere.

Figure 12 plots a synthetic spectrum from a snapshot of a hydrodynamic model with an extended pulsating

atmosphere and a dust-driven wind, alongside a spectrum of WBP 29. This model is based on the DARWIN code (Höfner et al. 2016) and is similar to the carbon-star models by Eriksson et al. (2023) and Siderud et al. (2025), except for the updated molecular opacities, as in the hydrostatic COMARCS models (see Section 4.2). While the dynamic simulations include dust, we have computed the synthetic spectrum without dust opacities. That choice makes the synthetic spectrum bluer, but it also removes dust as a possible cause of the apparent absorption at 10 μm. In the synthetic spectrum, the apparent dip at 10 μm is just continuum between molecular emission from other molecules to the red and to the blue. The 7.5 μm band can be seen in emission in Figure 12, as can the broad ν_5 C_2H_2 band with its Q branch at 13.7 μm and the P and R branches extending the band to ∼12 and 15 μm.

The similarity of the shape of the synthetic and observed spectra in the 10 μm region demonstrates that the emission scenario is plausible, but direct detailed evidence for emission on either side of the 10 μm feature is lacking. In WBP 29, C_2H_2, HCN, and CS are all detected between 7.0–7.5 μm, but in absorption. The absorption could arise from a cooler layer in the line of sight above the emitting layer. The same argument could also apply at 13.7 μm, where the ν_5 Q branch of C_2H_2 is clearly in absorption.

More work is needed on the nature of this apparent absorption band at 10 μm. If it is an absorption band, its presence is affecting the [6.4]−[9.3] color, which is used as a proxy for the ratio of dust to stellar emission and the dust-production rate. In Figure 6, the strong dip in the spectrum of WBP 29 at 10 μm appears to have driven the [6.4]−[9.3] color negative. Future work could mitigate this by shifting the 9.3 μm band to a shorter wavelength, perhaps ∼8.7 μm, which would move it partly out of the 10 μm dip.

Measurements of the SiC dust emission feature are also affected by the 10 μm dip to the blue, as well as absorption from C_2H_2 and other molecules to the red. At first glance, the synthetic spectrum in Figure 12 might look like it has SiC dust emission at ∼11.3 μm, but it does not. Leisenring et al. (2008) tried to address this challenge by modeling the "continuum" (from the star, amorphous carbon dust, and molecular absorption) when measuring the flux from SiC dust. A simpler approach would be to focus on the centroid of the extracted feature, as done in Section 4.1. While that might not remove all false positives, it would certainly catch some.

5.3. *MSX LMC 220 and Its Vanishing Dust Feature*

The dust emission in the spectrum of MSX LMC 220 has changed dramatically between the IRS and MRS epochs (Figure 5). The IRS spectrum shows a cool dust emission feature that peaks in the vicinity of 18 μm. We examined the spectral images from which the IRS spectrum was extracted and saw no evidence for a contaminating source or anything else unusual, leaving us to conclude that the earlier spectrum really does show this extra dust component. This feature could be related to an 18 μm shoulder seen in the dust emission from some carbon-rich planetary nebulae by Bernard-Salas et al. (2009), who noted that while it was in roughly the right position to be the O–Si–O bending mode in silicate dust, one would expect to see the Si–O stretching mode at 10 μm, which is absent, and oxygen-rich dust would be unlikely in a carbon-rich environment. They were unable to identify the carrier of the feature.

The disappearance of this apparent dust emission in the time between the IRS and MRS epochs is as much of a mystery as its origin in the first place. A simplistic calculation assuming blackbodies for the grains, radiative equilibrium in a stellar radiation field of $T_{\rm eff}$ = 3000 K for MSX LMC 220, and an outflow velocity of 10 km/s, results in changes in dust temperature too small for it to vanish from the infrared spectrum in the intervening 19.6 yr. For example, a grain at 150 K when observed by the IRS would have cooled to 140 K by the MRS epoch. A grain temperature as high as 1000 K is highly unlikely, but even then it would have cooled only to 380 K. MSX LMC 220 is the most luminous source in our sample, which raises the possibility that it is an unusual object and not a normal star on the AGB.

5.4. *Carbon Stars in the Early Universe*

The MRS enables the detailed study of the molecular gas in the envelopes of carbon stars, and that probes the chemistry of the gas from which carbon-rich dust condenses. The introduction noted that carbon stars likely contribute newly created dust to the early Universe, but they are often disregarded. Claims that the first carbon stars could not form until ∼1 Gy after the Big Bang (i.e., at a redshift of ∼5.7) have circulated for years (e.g., Todini & Ferrara 2001; Dwek et al. 2007). Instead, the alternative explanation has been supernovae (e.g., Maiolino et al. 2004; Dwek et al. 2007). However, the 1 Gyr delay for carbon star formation is outdated. Typically, ∼500 Myr are allowed for the first stars to form and another 500 Myr for carbon stars to form on the AGB. Both of those timescales are overestimates.

Regarding the first timescale, JWST has detected galaxies at $z > 14$, and spectra reveal emission from the optical [O III] doublet shifted into the mid-infrared

(e.g., Helton et al. 2026; Naidu et al. 2026). Since oxygen requires stellar nucleosynthesis, stars must have formed within 300 Myr of the Big Bang.

Regarding the second, stellar models show that metal-poor stars reach the AGB more quickly than their metal-rich analogs. For example, Vassiliadis & Wood (1993) found that at Solar metallicity, or $Z \sim 0.016$, a 2 $M_\odot$ star takes ∼1.6 Gy to evolve from the zero-age main sequence to the thermal-pulsing AGB, while the same star with $Z \sim 0.004$ takes 1.2 Gyr. Herwig (2004) found that at $Z = 0.0001$, a 2 $M_\odot$ star takes 800 Myr. At 5 $M_\odot$, the corresponding times are 123, 102, and 97 Myr.

A key question, though, is what the upper mass limit is for carbon stars at low metallicities. The cutoff is driven partly by proton capture at the bottom of the convective envelope, known as hot bottom burning, which converts carbon to nitrogen (Renzini & Voli 1981). Iben & Renzini (1983) noted that the creation of a carbon star on the AGB depends on the interplay between helium burning, dredge-up, proton capture, and details of the convection. More recently, the models of Straniero et al. (2023) suggest that the upper mass limit increases from ∼3 $M_\odot$ at Solar metallicity to > 5 $M_\odot$ at $Z = 0.002$. Although determining the upper mass limit for carbon stars remains a challenge, this work suggests that carbon stars could form early in the life of the Universe.

Combining our knowledge of how soon stars can form, 300 Myr, with the time a metal-poor 5 $M_\odot$ star takes to reach the thermal-pulsing AGB, 100 Myr, carbon stars could reasonably be expected to appear, and start creating dust, as early as 400 Myr after the Big Bang, or at a redshift of 11.4. Based on observations of metal-poor carbon stars in the Local Group (Sloan et al. 2012, 2016; Boyer et al. 2025) those earliest metal-poor carbon stars likely produced significant amounts of carbon-rich dust and ejected it back into their host galaxies.

5.5. *Molecular chemistry and metallicity*

This paper represents an initial assessment of the quality of the spectra and what they can reveal. The spectra are a complex blend of overlapping absorption bands from a multitude of carbon-bearing molecules, probably absorbing from multiple layers with different physical conditions, making them a challenge to model. The rewards of that modeling, though, promise to be rich. We can use chemical models and abundances of molecules like HCN and C_3 to determine the C/O ratio and probe isotopic ratios (e.g., $^{13}C/^{12}C$ and $^{15}N/^{14}N$) in gas dredged up from the nuclear-burning interior.

This paper has focused on the first results from a simplified spectral analysis method described as "flatten-and-fit." While this method avoids the complexities of detailed modeling, it comes with a number of caveats (as discussed in Section 4.2) which limit how quantitative conclusions can be. Nonetheless, it has strengthened the case for absorption from C_3, CS, and HCN. The presence of C_3 may require a shift in thinking from C_2H_2 as the only molecule dominating the mid-infrared absorption. The presence of CS and HCN point to the complexity of stellar enrichment at the metallicity of the LMC and raise the question of whether the MRS can detect these molecules at even lower metallicities.

Future work on this dataset will include more sophisticated analyses, to better disentangle the band structure and model the gas. That will probe the temperature and pressure of the absorbing molecules and better constrain the models. Improved understanding of the chemical and physical conditions in the circumstellar envelopes of the carbon stars will lead to improved understanding of the initial conditions for dust condensation. The current results for these nine carbon stars in the LMC demonstrate the capabilities of JWST's MRS to probe their properties more deeply than previous instruments and to reach even more metal-poor carbon stars that more closely resemble the carbon stars forming at high redshift.

6. SUMMARY

Observations of nine carbon stars in the LMC with the MRS reveal detailed molecular structure in their spectra. C_2H_2 produces strong and broad absorption bands centered at 7.5 and 13.7 μm that were well known before. Comparing the observed spectra structure to synthetic spectra from hydrostatic models of carbon stars reveals that CS is absorbing at ∼8 μm. The evidence for HCN is indirect, but including it in the fitted mixtures of absorptions from synthetic spectra in the wavelength intervals with C_2H_2 generally results in lower residuals in the fitting process. The MRS and synthetic spectra also support the identification of C_3 as the carrier of an absorption band centered at 5.2 μm, a result made possible by the improved wavelength coverage below 5 μm in the MRS compared to the IRS on Spitzer. The presence of C_3 explains the range of [5.8]−[8.0] colors observed in SRVs.

WBP 29 shows spectral structure that looks like a strong and broad 10 μm absorption band in the MRS data that is not apparent in the IRS epoch. This spectral structure appears in other spectra in our sample. A review of multi-epoch spectroscopy from the SWS on ISO confirms its presence and its variability in Galactic carbon stars. If the apparent 10 μm dip is an absorption band, its carrier is unknown. Hydrodynamic models of

carbon stars offer an alternative explanation, that we may be observing a continuum at 10 μm bracketed by emission at shorter and longer wavelengths. The variation appears to be related to the pulsation cycle of the star, with a stronger "dip" at 10 μm when the star is at optical maximum.

This variable spectral structure in the vicinity of the SiC dust emission feature at $\sim$11.3 μm raises some concern about the reliability of the measured dust emission strengths using the Manchester Method. That approach fits line segments above absorption bands and below emission features to estimate the continuum, but these spectra have no real continuum in the classic sense. For strong SiC emission, these problems are less significant, but detections of fainter SiC dust features may not be real. They may simply be continuum between absorption bands or shoulders between emission and absorption bands. We recommend that users of the Manchester Method use the measured central wavelengths of bands and features to identify possible false positives. It may also make sense to shift some of the continuum positions, such as the wavelengths used to measure the [6.4]$-$[9.3] color, which has served as a proxy for the amount of amorphous carbon dust contributing to the spectrum.

The spectrum of MSX LMC 220 changed significantly between the IRS and MRS epochs, with the older data showing a broad emission feature from apparent dust at $\sim$18 μm that is not present in the MRS data. The origin of the feature in the previous epoch and the reason for its disappearance are not known.

The authors thank the anonymous referee for thoughtful feedback that resulted in an improved manuscript. Support for G.C.S., K.E.K., E.J.M., and R.S. was provided through grant JWST-GO-03010.005 under NASA contract NAS5-03127. B.A. and S.H. acknowledge funding from the European Research Council (ERC) under the European Union's Horizon 2020 research and innovation program (grant agreement No. 883867, project EXWINGS) and the Swedish Research Council (Vetenskapsradet, grant no. 2019-04059). J.C. acknowledges support from the University of Western Ontario and the Natural Sciences and Engineering Research Council of Canada. K.J. is supported by the Swedish National Space Agency, and M.M. is supported by STFC consolidated grant (ST/W000830/1). I.M. and A.A.Z. acknowledge funding from the OSCARS project, which has received funding from the European Commission's Horizon Europe Research and Innovation program under grant agreement No. 101129751. The contribution of R.S. to the research described here was carried out at the Jet Propulsion Laboratory, California Institute of Technology, under a contract with NASA (80NM0018D0004).

We gratefully acknowledge the observations of variable stars from the International Database of the American Association of Variable Star Observers (AAVSO) contributed by observers around the world. Some of the observations used here were obtained by the British Astronomical Association for Variable Star Section. This research has made use of the VizieR catalog access tool at the Strasbourg Astronomical Data center (CDS) in Strasbourg, France (Ochsenbein et al. 2000), the Astrophysics Data System (ADS) funded by NASA under Cooperative Agreement 80NSSC25M7105 at the Smithsonian Astrophysical Observatory, and the Infrared Science Archive (IRSA) operated by IPAC at the California Institute of Technology. It has also utilized data from the Gaia mission of the European Space Agency (ESA; https://www.cosmos.esa.int/gaia), processed by the Gaia Data Processing and Analysis Consortium (DPAC) and funded by the institutions participating in the Gaia Multilateral Agreement.

Coauthor Paola Marigo died while this program was still obtaining observations. Her work strongly contributed to the success of our observing proposal, and we deeply regret that we did not have the opportunity of analyzing and interpreting the spectra alongside her.

Facilities: AAVSO, ISO (SWS), Spitzer (IRAC, IRS), WISE, JWST (MIRI, MRS)

APPENDIX

A. INFRARED LIGHT CURVES

We can use multiepoch infrared photometry to determine the phase of the pulsational cycle of the stars when the IRS and MRS obtained spectra. We constructed light curves for all nine targets using 3.6 and 4.5 μm photometry from the SAGE and SAGE-Var surveys and 3.4 and 4.6 μm photometry from WISE. Most of the targets have 29 epochs, two from SAGE in 2005, four from SAGE-Var in 2010 and 2011, two from the original WISE mission in 2010, and 21 from the reactivated WISE mission, NEOWISE-R, which ran from 2014 to mid-2024.

The WISE epochs are spaced roughly 6 months apart. Each of these epochs consists of many individual scans obtained every few hours. Because the LMC is close to the south ecliptic pole, targets in the sample had an average of between 174 and 391 of these individual scans per epoch. The photometry from the individual scans was combined by finding a median, filtering out any data more than 0.35 magnitudes from that value, then redetermining the median.

The SAGE and SAGE-Var data provide epochs that are not on the 6 month cadence of the WISE data, so they can help break degeneracies. The SAGE-Var data were taken contemporaneously with the first two original WISE epochs, making them particularly helpful, and the SAGE epochs in 2005 extend the photometric baseline to 19 yr.

The IRAC data require a correction to align with the WISE data. The first part of the correction is based on the color corrections generated by Sloan et al. (2016), except that they converted from WISE to IRAC. We repeated their analysis, going in the other direction and adding the WISE epochs since 2016 to the analysis. Table 5 gives the results, based on least-squares fits of lines to the mean magnitudes for all of the carbon stars in the Spitzer/IRS sample defined by Sloan et al. (2016). That sample includes 184 carbon stars in the LMC and 40 in the SMC. Stars with [3.6]−[4.5] colors > 1.55 were excluded, because the color corrections for the reddest carbon stars do not appear to follow any coherent trend.

The corrections in Table 5 leave the IRAC data still offset from the WISE data by typically ∼0.15–0.25 mag. These offsets are within the scatter of the photometry for the full sample (see Figure 17 from Sloan et al. 2016), and they are generally unimportant when fitting the large-amplitude variables at the red end of the Mira sequence. For weaker pulsations, though, the offsets make using the IRAC data challenging.

To remove these residual offsets, we first fitted a sinusoid to just the WISE photometry, then used that to determine the mean residuals for the IRAC photometry after the first correction was applied. The second correction to the IRAC photometry then removed those offsets source by source. As explained below for individual stars, two stars show long-term variations in their light curves in addition to the fitted sinusoid, and for those we forced the average residuals for the four SAGE-Var and two original WISE epochs, all taken in 2010–2011, to match.

Our algorithm for fitting light curves is based on the one used by Sloan et al. (2016). We iterated through pulsation periods, typically from 100 to 1200 days, with a step size of 1 day, fitted a sine function to the W1 and W2 data independently, and picked the period with the least χ^2 residuals for each. The pulsation periods for W1 and W2 were then averaged, and sinusoids were fitted to determine the mean magnitudes and amplitudes for W1 and W2. That result served as the basis for determining the second correction to the IRAC photometry.

With the IRAC photometry corrected to be consistent with WISE, we then fitted sinusoids to the combined IRAC and WISE photometry, again iterating from 100 to 1200 days and searching for the period with the minimum residuals. Table 6 gives the results. The reported period is the average from fitting W1 and W2 separately, and the mean magnitudes and amplitudes were determined by using that mean period. The amplitudes are peak-to-peak for the fitted sinusoid. The uncertainty in period is the standard deviation of the four periods found for W1 and W2 with and without using the IRAC photometry, illustrating how the measured periods depend on the data available. The zero-phase epoch is the average of the results for W1 and W2 in the final fitting step (fixed period, IRAC and WISE data), and the quoted uncertainty is the uncertainty in the mean (i.e., half the difference).

Table 6 gives the periods to nearest day, given the uncertainties of ∼1–5 days. Figures 13 to 15 show the light curves and fitted sinusoids for both unphased and phased data, and Figure 16 plots the residuals from the fitted sinusoids (data − model). The following subsections discuss the results for each star.

Table 5. Color and Magnitude Corrections for Carbon Stars

Relation	y-intercept	Slope
(W1−W2) − ([3.6]−[4.5]) versus [3.6]−[4.5]	0.1528	0.3003
W1−[3.6] versus [3.6]−[4.5]	0.0352	0.3449
W2−[4.5] versus [3.6]−[4.5]	−0.0224	0.0537

NOTE—These corrections are only valid for [3.6]−[4.5] < 1.55.

Table 6. Fitted Light Curves

	Pulsation	Mean		Amplitude[a,b]		Mean	IRAC Offsets[c]		Phase When	
	Period[a]	Magnitude		(mag)		Zero-phase	(mag)		Observed by	
Target	(d)	W1	W2	W1	W2	MJD	W1	W2	IRS[a]	MRS[a]
J050629	(218 ± 0.8)	10.456	10.519	0.090	0.077	53845.5 ± 3.0	−0.217	−0.135	(0.93)	(0.48)
KDM 1691	523 ± 1.2	9.065	9.010	0.174	0.143	53364.4 ± 2.9	−0.214	−0.034	0.46	0.74
WBP 17	309 ± 2.0	10.400	10.319	0.269	0.216	53608.5 ± 0.7	−0.146	−0.072	0.96	0.47
WBP 29	245 ± 0.8	10.705	10.584	0.367	0.268	53654.7 ± 0.9	−0.179	−0.269	0.30	0.02
J051803	372 ± 4.7	9.803	9.212	(0.296)	(0.234)	53091.1 ± 7.0	0.013	0.128	0.29	0.89
J053441[d]	519 ± 2.9	8.970	8.070	0.408	0.391	55434.0 ± 4.7	−0.161	0.015	0.40	0.85
MSX LMC 220	637 ± 4.5	8.528	7.292	1.131	1.055	53685.4 ± 0.6	0.217	0.266	0.52	0.78
MSX LMC 774	671 ± 1.7	9.716	8.100	1.312	1.126	53831.5 ± 0.9	−0.138	−0.005	0.43	0.01
MSX LMC 736	690 ± 1.4	10.740	8.803	1.138	1.120	53472.9 ± 0.6	−0.123	0.005	0.64	0.02

[a] Values in parentheses are poorly constrained.

[b] The peak-to-peak amplitude of the fitted sinusoid.

[c] Offsets should be subtracted from the IRAC photometry after the first correction.

[d] The results are from the light curve fitted to just the WISE photometry.

A.1. *J050629*

J050629 is classified as an SRV, and it behaves like one, with a small pulsation amplitude and no clear pulsation period, resulting in inconsistent periods in the literature. The OGLE-III survey reported two periods, 741.3 and 154.42 days with similar amplitudes (Soszyński et al. 2009), while survey for Massive Compact Halo Objects (MACHO) reported periods of 266.52 and 238.49 days, again with similar amplitudes (Fraser et al. 2005). Sloan et al. (2024) published a light curve with a period of 154 days, consistent with the shorter OGLE-III period.

The present analysis includes one more WISE epoch than available to Sloan et al. (2024). Adding it and improving the corrections to the IRAC photometry result in two possible pulsation periods, 156 or 218 days. The combined χ^2 residuals for W1 and W2 are smaller for the 218 day period, and that is what is reported here. No one period dominates the light curve of this star. The different published periods may well result from what mode, or resonance between modes, happened to be strongest at the time each survey obtained its data. We can say little about the relative phases of observations for this star, but the pulsation amplitudes are small, so that the star was likely to have been in a similar physical state for both observations.

A.2. *KDM 1691*

KDM 1691 is an SRV, like J050629, but the literature gives a more consistent period of somewhere over 500 d, with reported periods of 502.77 (Soszyński et al. 2009), 518.7 (Fraser et al. 2005), 529 (Groenewegen & Sloan 2018), and 531.95 days (Kim et al. 2014), to take some examples from the literature. However, both the OGLE-

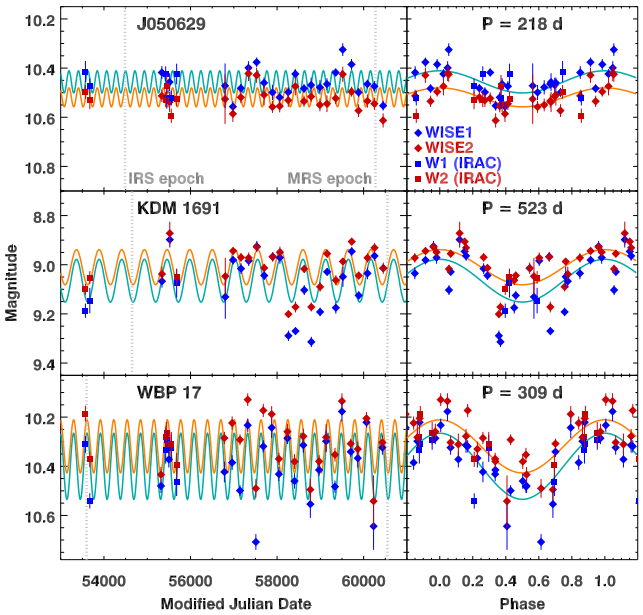

Figure 13. Light curves for the three SRVs in the sample, plotted versus MJD (left) and phased (right). IRAC data color-corrected to the WISE filters are plotted as squares. The fitted sine functions are plotted in light blue for W1 and orange for W2. In the left-hand panels, the vertical dashed lines give the epochs of the IRS and MRS observations. All three panels have the same vertical range, 0.75 mag.

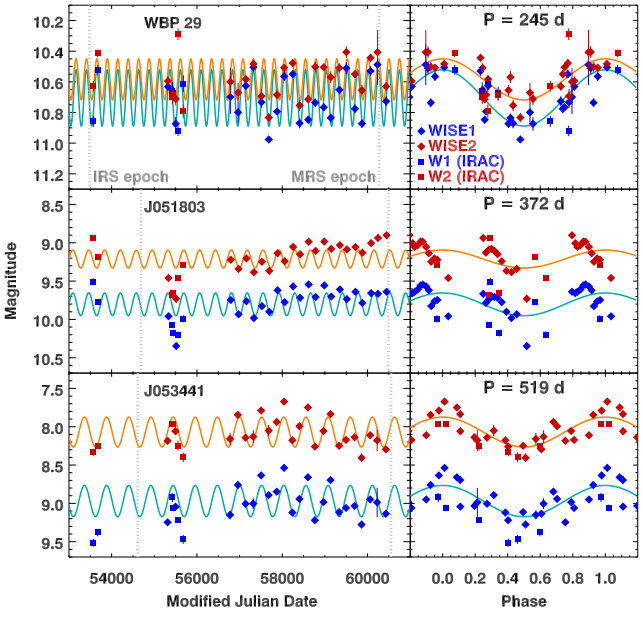

Figure 14. Light curves for the three bluest Miras in the sample. The figure key is the same as Figure 13. The top panel has half the magnitude range of the bottom two (1.2 mag versus 2.4 mag). The nearly 1 yr period of J51803 and the 6 month cadence of the WISE data mean that the fitted pulsation amplitudes are not trustworthy.

III and MACHO surveys reported weaker overtone periods of 285.8 and 261.37 days, respectively, indicating that the pulsations are not particularly stable.

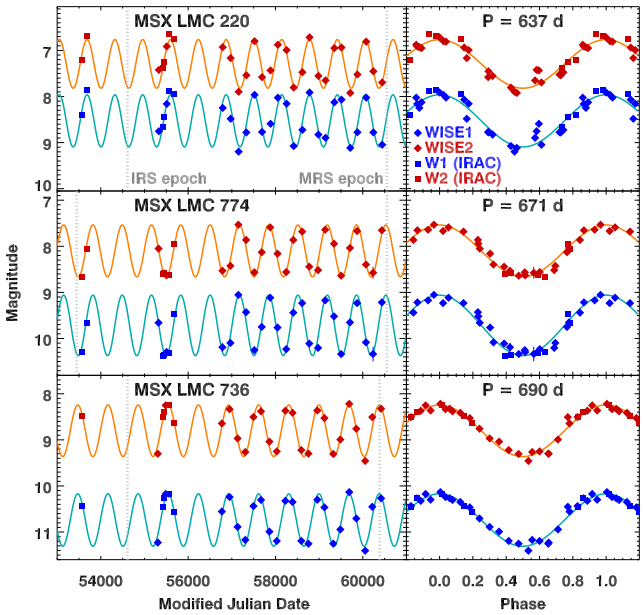

Figure 15. Light curves for the three reddest Miras in the sample. The figure key is the same as for Figure 13. All three panels have a vertical extent of 4 mag.

Analyzing the WISE data reveals multiple possible periods, at 135, 170, 197, 279, and 522 days, with minimum χ^2 residuals at 197 days for W1 and 522 days for W2. Such complex pulsational behavior should be expected for an SRV. The 522 d period is more consistent with the optical results, and because this star is not reddened by much dust and the optical data have a much better cadence, it is reported here.

The amplitudes of the pulsation cycles in KDM 1691 are twice those of J050729, but they are still less than 0.2 mag, making this star a weak pulsator, despite the apparently long pulsation period. The light curve in Figure 13 and the residuals in Figure 16 show that the pulsation cycle is more complex than a single sinusoid, with a notable excursion to fainter magnitudes between MJD 58000 and 59000 (2017–2020). All of the above is behavior expected for an SRV. Nonetheless, the pulsation period is long enough and characterized well enough that we can state confidently that the star was observed close to its minimum by the IRS and halfway between minimum and maximum by the MRS.

A.3. *WBP 17*

WBP 17 is the third SRV in the sample, and its period is consistently close to 310 days in the literature. The OGLE-III survey reported 314.3 days (Soszyński et al. 2009) and the MACHO survey reported 308.45 days (Fraser et al. 2005). Ou & Ngeow (2022) reanalyzed the

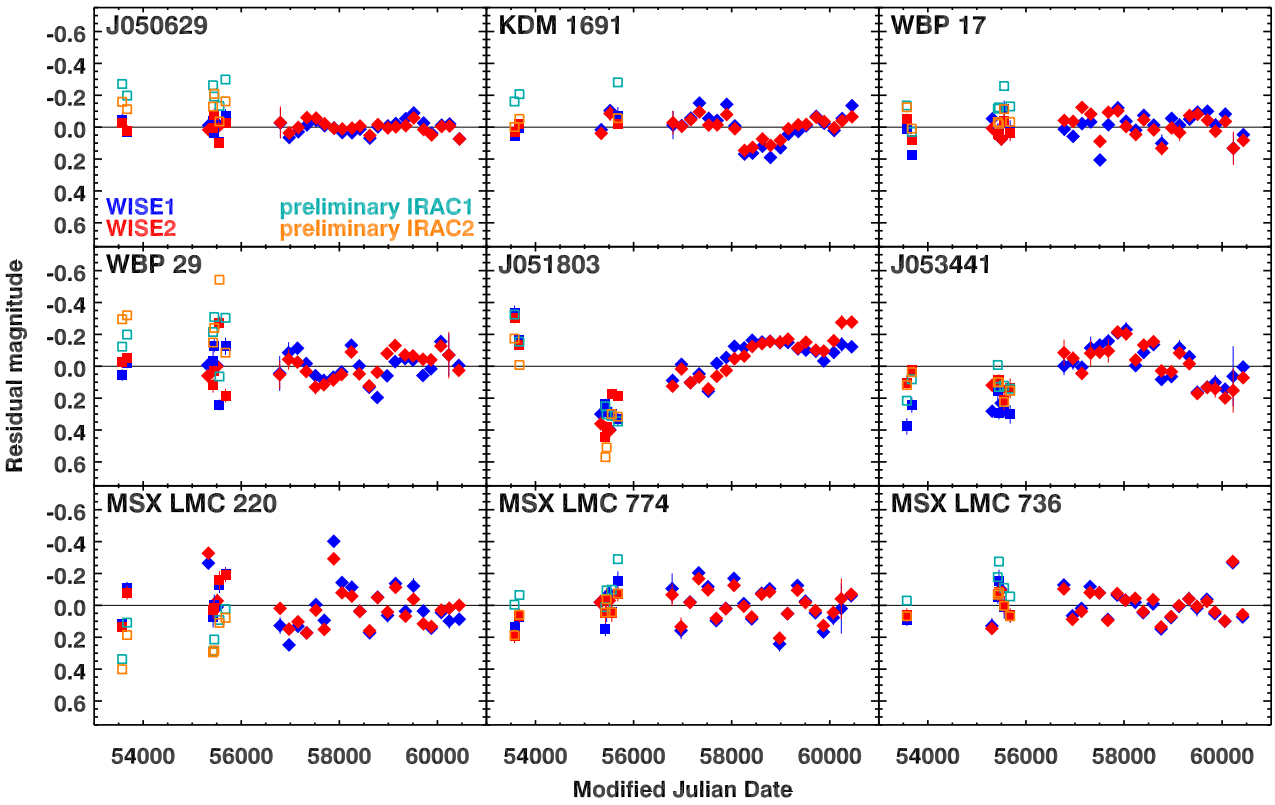

Figure 16. Residuals after subtracting the fitted sinusoids from the observed light curves, with diamonds for WISE observations and squares for color-corrected IRAC data. The IRAC data after the color corrections in Table 5 are plotted as open squares in light blue (for IRAC1) and orange (for IRAC2). The corresponding data after correcting for the residual offsets in Table 6 are plotted as blue or red closed squares.

OGLE-III data and found a period of 315.44 days. Our analysis suggests that pulsation periods of 244 and 309 days fit the light curves with similar residuals, but the optical data are more finely sampled. Consequently, we report the period closest to ∼310idays.

The pulsation amplitudes of WBP 17 are the strongest of the three SRVs in the sample, but evidence for some irregularities in its behavior can still be seen in its light curve and its residuals at a level of ∼0.2 mag. Despite those deviations from a sinusoid, the light curve is clean enough to show that the IRS observation came close to maximum and the MRS observation close to minimum.

A.4. *WBP 29*

WBP 29 is the least reddened of the six Miras in the sample, and it also has the shortest pulsation period, with OGLE-III reporting 246.7 days (Soszyński et al. 2009) and MACHO reporting 245.82 days (Fraser et al. 2005). Seven other investigators found periods between 240 and 247 days (Groenewegen 2004; Ita et al. 2004; Spano et al. 2011; Kim et al. 2014; Groenewegen & Sloan 2018; Iwanek et al. 2021). Our analysis of the IRAC and WISE data results in a period of 245 days. The fitted light curves imply that the IRS observation was obtained approaching minimum and the MRS observation at maximum.

A.5. *J051803*

Previous studies indicate a pulsation period for J051803 close to 1 yr. Soszyński et al. (2009) found that the strongest pulsations had a 348.9 day period, Groenewegen & Sloan (2018) reported 352 days, and (Iwanek et al. 2021) reported 362.44 days. A period close to 1 yr is particularly difficult for the WISE cadence, but the IRAC epochs may have broken the degeneracy. For the first pass, instead of using WISE data to find a period, we adopted the period of 362.44 day and used that to determine the corrections for the IRAC photometry.

The light-curve residuals for J051803 in Figure 16 indicate that the star has long-term variations, with a peak-to-peak amplitude of ∼0.5 mag. To avoid the impact of this long-term trend, we determined the corrections to the IRAC data using the four SAGE-Var epochs and the two WISE epochs in the interval 55000 < MJD < 56000. Combining the corrected IRAC photometry with WISE gives a pulsation period of 372 days. This pulsation period is still close to a year, and the full pulsation cycle is poorly sampled by the IRAC and WISE photometry.

For that reason, the pulsation amplitude is poorly constrained, as indicated in Table 6.

The fitted periods for J051803 have been increasing with time, but whether this result is meaningful or not is an open question. The zero-phase epoch for the fitted sinusoids differs by 14 days between W1 and W2, the largest difference for the stars in our sample. That might be a result of a period close to 1 yr, or it could arise from the long-term variations. The residuals show a hint of periodicity, but the available data do not constrain a possible period well. Fitting both the WISE data and the corrected IRAC data yields a period of ∼6140 days in W1 and ∼7130 days in W2, which is a rather significant difference of ∼15%. While the period may not be well constrained, the peak-to-peak amplitude of a sinusoid fitted to these residuals is significant: 0.93 mag in W1 and 1.0 mag in W2. These long-period results should be viewed more as suggestions than meaningful measurements. With all of these uncertainties, the only safe conclusion is that J051803 has a complex light curve.

The fitted light curve for J051803 suggests that the IRS epoch was obtained as the source was roughly halfway from maximum to minimum and the MRS epoch was approaching maximum. But all the caveats for the light curve for this source should be kept in mind.

A.6. *J053441*

J053441 has a light curve similar to J051803, except that the primary pulsation period is considerably longer than one year. Previous investigations found periods between 489 and 548 days (Soszyński et al. 2009; Spano et al. 2011; Groenewegen et al. 2020; Iwanek et al. 2021; Ou & Ngeow 2022). Our analysis of the WISE photometry results in a period of 519 days. As with J051803, the light curve shows long-term variations (see Figure 16), forcing us to determine a correction for the IRAC data using just the data with 55000 < MJD < 56000. Despite those corrections, adding the IRAC data did not help us determine a primary period, because the curve-fitting software failed to converge at the minimum χ^2 residuals in W2. The period in W1 was 522 days, and that in W2 at least 523 days. Table 6 gives the results for just the WISE data, although the uncertainty in the period reflects the range in the fitted period introduced by adding the IRAC data.

J053441, like J051803, shows possible periodicity in its residuals. Fitting both the WISE data and the corrected IRAC data gives periods of ∼7700 days for W1 and ∼5700 days for W2, but the discrepancy between the two filters is even larger than for J051803. The peak-to-peak amplitudes are smaller: 0.90 mag in W1 and 0.57 mag in W2. The long-term variations are clear enough, but the available data do not allow them to be properly quantified.

A.7. *MSX LMC 220*

For MSX LMC 220, we find a period of 644 days with just the WISE data. Adding the corrected IRAC data shifts this result to 637 days. Previous results have similar periods of 625 and 632 days (Groenewegen et al. 2009; Groenewegen & Sloan 2018), although OGLE-III reported periods of 313 and 1805 days (Soszyński et al. 2009). The light curves based on the IRAC and WISE data indicate fairly steady pulsations over the past 20 yr in the 3–5 μm range (Figure 14), but the residuals in Figure 16 show deviations of up to ∼0.4 mag in some isolated epochs, suggesting that the pulsations are not completely settled. The pulsation cycle is long enough and the pulsations steady enough to conclude with some confidence that the IRS epoch came close to minimum, while the MRS epoch came as MSX LMC 220 was roughly halfway to maximum.

A.8. *MSX LMC 774*

Moving to the red end of the Mira sequence leads to steadier and stronger pulsations, and MSX LMC 774 follows that trend. Its dust shell effectively erases the star from the optical skies, so it does not appear in the OGLE-III and MACHO surveys. Using the IRAC data and the limited number of WISE epochs available at the time, Sloan et al. (2016) found a period of 670 days, and with more epochs and a slightly different technique, Groenewegen (2022) found periods of 680 days in W1 and 678 days in W2. Using even more WISE epochs, we find a period of 668 days. The well-behaved pulsation cycle and long period of MSX LMC 774 constrain the epochs of the IRS and MRS spectroscopy well, with the IRS observing the star just before minimum and the MRS very close to maximum.

A.9. *MSX LMC 736*

MSX LMC 736 is another Mira too reddened by its own dust to appear in optical variability surveys. Previous measurements of its period have been based on the six SAGE and SAGE-Var epochs and increasing numbers of epochs from WISE: 686 (Sloan et al. 2016), 683 (Groenewegen & Sloan 2018), 672 (Groenewegen et al. 2020), and 690 days (Sloan et al. 2024). This work duplicates the last period, 690 days, even though it adds one WISE epoch and corrects the IRAC photometry for residuals. As with MSX LMC 774, the light curve constrains the IRS and MRS epochs well, with the first just after minimum and the second right at maximum.

B. LUMINOSITIES

Table 7 presents bolometric luminosities for the stars in our sample, determined using two methods and compared to the results from Groenewegen & Sloan (2018). Our first method is to apply the PySSED software (version 1.1), which constructs a spectral energy distribution (SED) for a source from an automated lookup of the available photometry in VizieR and integrates the result through wavelength space (McDonald et al. 2024, 2025). Our second method of determining the bolometric luminosity uses a curated set of photometry and the spectra from the IRS and MRS.

For the second (curated) method, the mid-infrared photometric data were limited to the mean 24 μm photometry from the SAGE survey (Meixner et al. 2006) and the mean results in the WISE filters at 3.4 and 4.6 μm reported in Appendix A (including the color-corrected IRAC photometry from SAGE and SAGE-Var). We also used near-infrared photometry from the Two Micron All Sky Survey (2MASS; Skrutskie et al. 2006), 2MASS 6X (same reference), photometry from the Infrared Spectral Survey (Kato et al. 2007), the Deep Near Infrared Survey of the Southern Sky (DENIS; Cioni et al. 2000), and the Vista Magellanic Cloud (VMC) survey DR6 (Cioni et al. 2011). Photometry at shorter wavelengths came from the OGLE-III survey (Soszyński et al. 2009), the MACHO survey (Fraser et al. 2008), the Magellanic Clouds Photometric Survey (MCPS; Zaritsky et al. 2004), the SkyMapper Southern Sky Survey DR4 (Onken et al. 2024), and Gaia DR3 (Gaia Collaboration 2023). We did not include the K_s photometry from the VMC because it gave the faintest magnitude at K_s in five of the nine sources. We omitted the MACHO R_c magnitudes, because they were low outliers in all four sources for which data were available. We also omitted the MCPS i-band data for J053441 and MSX LMC 220 because they were outliers and one of the DENIS I-band magnitudes for MSX LMC 220 for the same reason. For both J051803 and MSX LMC 736, some care was required to avoid neighboring sources. We averaged the remaining data at I (0.77–0.80 /um), J (1.22–1.25 μm), H (1.61–1.67 μm), and K_s (2.23–2.16 μm).

We combined the MRS and IRS data by regridding the MRS to the IRS, truncating the MRS beyond 20 μm, averaging the spectra where they overlapped, and normalizing the remaining spectral data to align with the average. To normalize the resulting spectra to the approximate mean of the light curve, we used the phase information for the epochs in Appendix A. For six of the nine carbon stars, we forced the combined spectrum to the average of the two. The exceptions were KDM 1691 and MSX LMC 220, where we forced the IRS to align with the MRS, and J051803, where we did the opposite. Figure 17 shows the resulting SEDs for all nine sources, along with the spectra from the MRS and IRS.

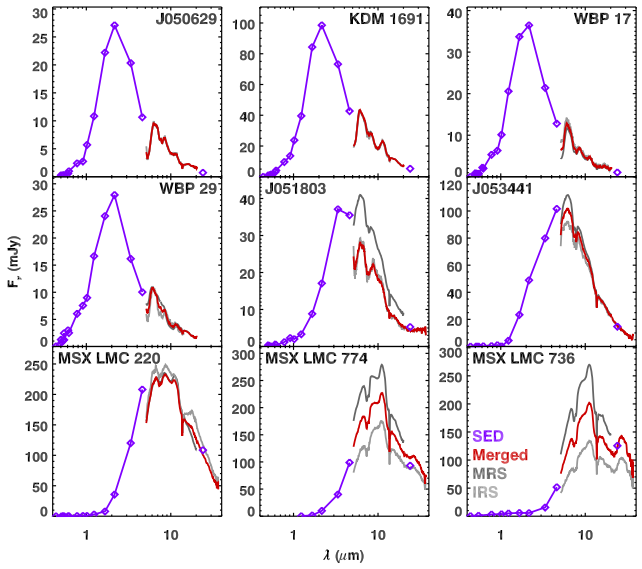

Figure 17. SEDs and merged spectra from the MRS and IRS for the nine stars in the sample. The plotted data are not corrected for interstellar absorption.

The PySSED code uses Gaia-based extinction maps from Lallement et al. (2022). Groenewegen & Sloan (2018) assumed $A_v = 0.15$ in the LMC, and we followed their lead. We used the interstellar extinction from Rieke & Lebofsky (1985) to 1.35 μm and that from Chiar & Tielens (2006) past 1.35 μm. The extinction affected the results by ∼3% for the bluer sources and ∼1%–2% for the redder sources, meaning that the specific choice for the extinction correction has little effect.

We integrated the combination of SED and spectra to determine the bolometric luminosity of each source, using a Wien tail for a 3000 K blackbody to extrapolate to the blue from the shortest observed wavelength and a Rayleigh-Jeans tail to extrapolate from the longest observed wavelength to the red. For the three SRVs and WBP 29, the usable spectral data only extended as far as 20 μm, so we included the MIPS 24 μm photometry in the SED. For the remaining five Miras, the spectral data extended to 38 μm and we omitted the MIPS photometry.

For the luminosities and bolometric magnitudes, we assumed a distance modulus to the LMC of 18.48 mag (Pietrzyński et al. 2019). We shifted the results from Groenewegen & Sloan (2018) to this distance; they assumed a distance of 50.0 kpc ($m - M = 18.495$ mag).

Table 7. Bolometric Luminosities and Magnitudes

Target	Bolometric Luminosity ($L_\odot$)				M_{bol} (mag)
	Groenewegen & Sloan (2018)[a]	PySSED Method	Curated SED and Spectra	Mean[b]	
J050629	(3489)	3818	3824	3821 ± 3	−4.21 ± 0.00
KDM 1691	12,707	13,595	14,653	13,652 ± 562	−5.59 ± 0.04
WBP 17	(7268)	5201	5824	5513 ± 312	−4.60 ± 0.06
WBP 29	5032	5084	4910	5009 ± 52	−4.50 ± 0.01
J051803	(4851)	2968	3570	3269 ± 301	−4.04 ± 0.10
J053441	8198	10,232	9145	9192 ± 588	−5.16 ± 0.07
MSX LMC 220	(23,388)	16,290	15,230	15,760 ± 530	−5.74 ± 0.04
MSX LMC 774	7574	7342	9620	8179 ± 723	−5.03 ± 0.10
MSX LMC 736	9311	7168	8150	8210 ± 619	−5.04 ± 0.08

[a] Values not used in mean luminosity are in parentheses.

[b] The uncertainties are the uncertainty in the mean.

As Table 7 shows, the PySSED method generally obtained similar results to the combination of curated SEDs and MRS and IRS spectra, in no small part because both methods shared much of the same photometry. Given the work involved in curating the photometry, the similar results are a strong argument for using the more automated PySSED method. Groenewegen & Sloan (2018) used the photometry available at that time to construct a model of the star and from that determined the bolometric luminosity. That method produced results that differed more significantly. We excluded the model-based luminosities when they doubled the standard deviation estimated from our two methods (Table 7 shows the excluded values in parentheses). The remaining five luminosities were averaged with the results from our two methods to provide the mean luminosities in Table 7 (and Table 1).

C. FITTING THE BAND STRUCTURE IN THE SPECTRA

The figure set of Figure 18 compares the flattened spectra of the carbon stars in our sample to the best-fitting combination of absorbing molecules, using synthetic spectra generated from a 2800 K model for the SRVs and from 3100 K for the Mira variables. The plotted spectra cover the eight wavelength intervals defined in Section 4.2. The observed spectra are corrected for the radial velocities determined in Section 4.2.1 and listed in Table 3.

D. MULTIEPOCH SPECTRA FROM ISO

The SWS on ISO obtained reliable infrared spectra of 42 Galactic carbon stars (Leisenring et al. 2008; Sloan et al. 2016). Several of these stars were observed multiple times, and we examined the individual spectra of all of them for variations in the apparent 10 μm absorption band, using the spectra processed by Sloan et al. (2003). Four sources showed this apparent absorption, and it varied in each of them.

Table 8 provides basic information about the four Galactic carbon stars, including their [6.4]−[9.3] colors, which range from ∼0.3 to ∼0.5. That interval includes the MRS targets J051803 and J053441. R Scl is an SRb variable, and the other three are Miras. The pulsation periods range from ∼360 to 480 days, again similar to J051803 and J053441.

Table 9 gives the details of each SWS observation considered. Two observations of R Scl and V CrB occurred on the same day; we treated these independently, but they corroborate each other well.

To check the spectral variations with the pulsation phase, we analyzed visual photometry of the four Galactic carbon stars from the American Association of Variable Star Observers (Kloppenorg 2025). We excluded upper limits and data described as "discrepant." Figure 26 plots the AAVSO light curves, and it also shows when the SWS data were obtained. For each SWS epoch, we estimated a visual magnitude by averaging the AAVSO data within an interval of ±20 days. While S Cep has only two epochs, compared to six to seven

Table 8. Comparison Carbon Stars in the Galaxy

Target	R.A.	Decl.	Spec.	Spec.	Variability[c]		[6.4]−[9.3][d]
			Type	Ref.[b]	Type	Period	
	(J2000)[a]					(days)	(mag)
R Scl	21.783725	−32.801921	C6.4p	S44	SRb	370	0.27
V CrB	237.380467	+39.571637	C6,2e	S44	Mira	357.63	0.40
V Cyg	310.326115	+48.141336	C5,3e	Y75	Mira	421.27	0.52
S Cep	323.803430	+78.624496	C6.3e	Y75	Mira	484.4	0.30

[a] From Gaia EDR3 (Gaia Collaboration 2021).

[b] S44 = Sanford (1944); Y75 = Yamashita (1975).

[c] Samus et al. (2017).

[d] Leisenring et al. (2008).

Table 9. SWS Observing Log

Target	TDT[a]	Obs. Date
		(MJD)
R Scl	24701012	50285
	37801213	50414
	37801443	50414
	39901911	50436
	41401514	50451
	56900115	50606
V CrB	11105149	50149
	25502252	50293
	42200213	50459
	42300201	50460
	47600302	50513
	57401003	50611
	67600104	50712
V Cyg	08001855	50118
	42100111	50458
	42300307	50460
	51401308	50551
	59501909	50632
	69500110	50731
S Cep	56200926	50599
	75100424	50787

[a] Time Designated Target number. The first three digits give the approximate number of days since the launch of ISO.

epochs each for the other three stars, they fall conveniently close to a visual maximum and minimum.

Figure 27 plots the individual spectral observations from the SWS. The first and last observations of R Scl, both taken at or close to maximum, show stronger apparent absorption at 10 μm than the four observations taken as the star approached minimum. The correlation of the strength of the band with phase is strong, with the two observations closest to minimum showing the weakest apparent absorption. S Cep shows the same dependency of apparent 10 μm absorption with phase, with the caveat that we only have two epochs.

If we had the same two observations of V Cyg, we could expect to draw a similar conclusion, with the last epoch coming at maximum and showing deep apparent 10 μm absorption, and the fourth epoch (gold) coming at minimum and showing the weakest apparent absorption. The remaining epochs, however, do not follow such a consistent pattern, with the second and third epochs (blue and green) obtained as the star approached minimum and showing almost as much apparent absorption as when the star was at maximum. V CrB also shows complex behavior. While the epochs closest to minimum are among the spectra with the weakest apparent absorption (green, gold, and brown), and the epoch closest to maximum among the strongest (red), the epochs at intermediate phases do not appear to follow a coherent pattern.

We conclude that the SWS data confirm the presence of a varying apparent absorption component at 10 μm in the spectra of carbon stars observed with the MRS, and that the trend is generally for stronger apparent

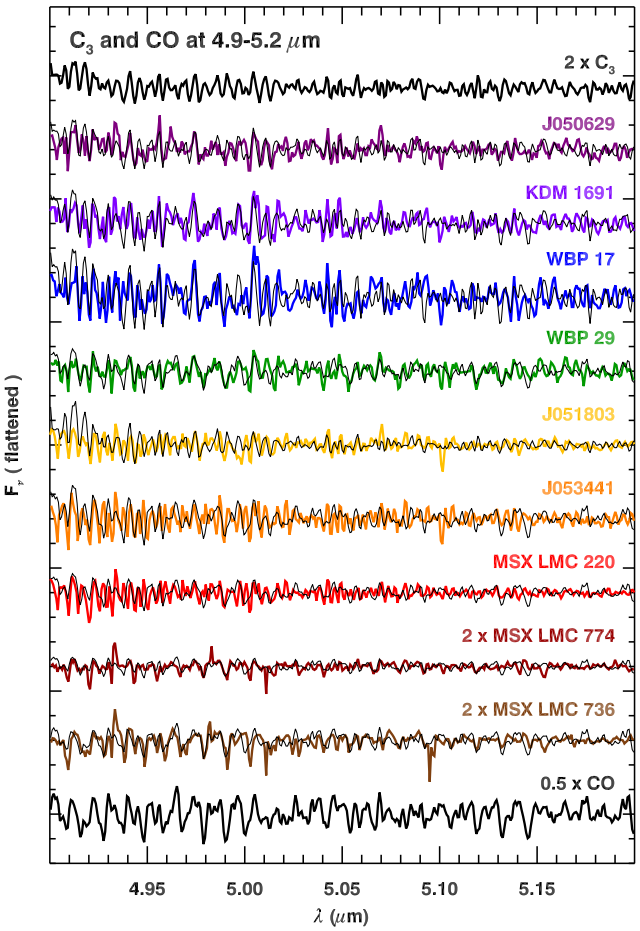

Figure 18. The flattened spectra at 4.9–5.2 μm for the nine carbon stars in the sample (in color) and the best-fitting combination of molecular spectra for each (black). The C_3 spectrum at the top is from the synthetic spectrum based on an effective temperature of 3100 K. The CO spectrum at the bottom is for 2800 K. Both are for a C/O ratio of 2.0. The observed spectra are shifted to correct for the radial velocities in Table 3. This figure will be part of a figure set of 8 images in the published paper.

absorption when the central star is at its maximum in the optical.

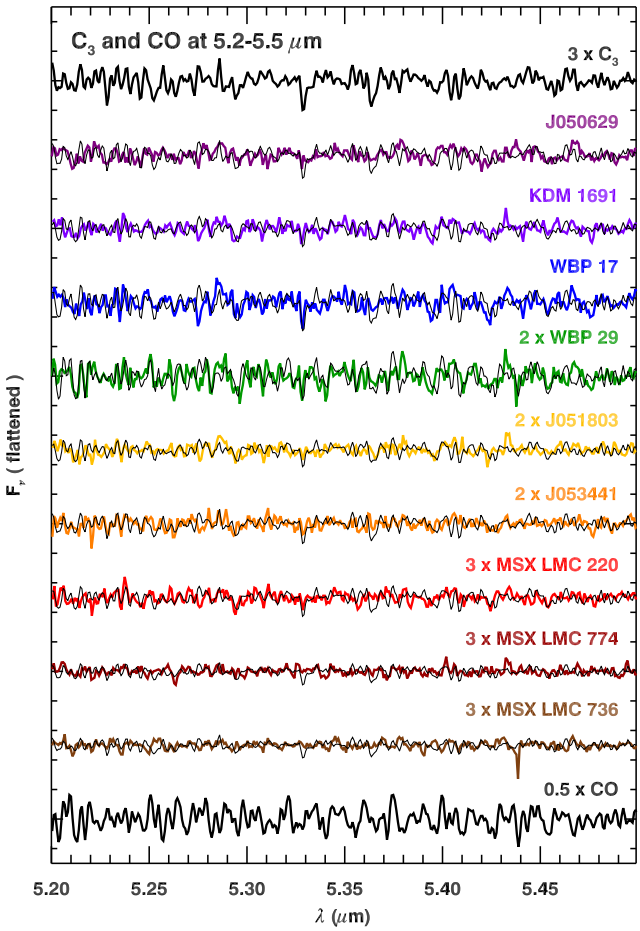

Figure 19. As Figure 18, but for 5.2–5.5 μm. This figure will be part of Figure Set 18 in the published paper.

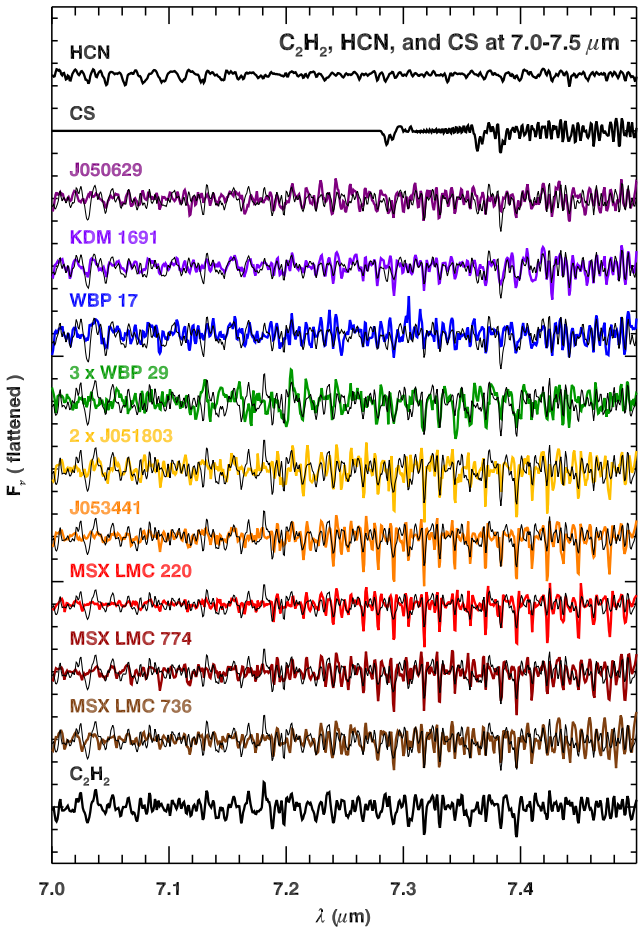

Figure 20. The flattened spectra at 7.0–7.5 μm, with the observed spectra in color and the fitted molecular spectra in black. The HCN and CS at the top are from the synthetic spectra with $T_{\rm eff}$ = 3100 K, and the C_2H_2 at the bottom is from the 2800 K spectrum. Both have a C/O ratio of 2.0. The observed spectra are corrected for the radial velocities in Table 3. This figure will be part of Figure Set 18 in the published paper.

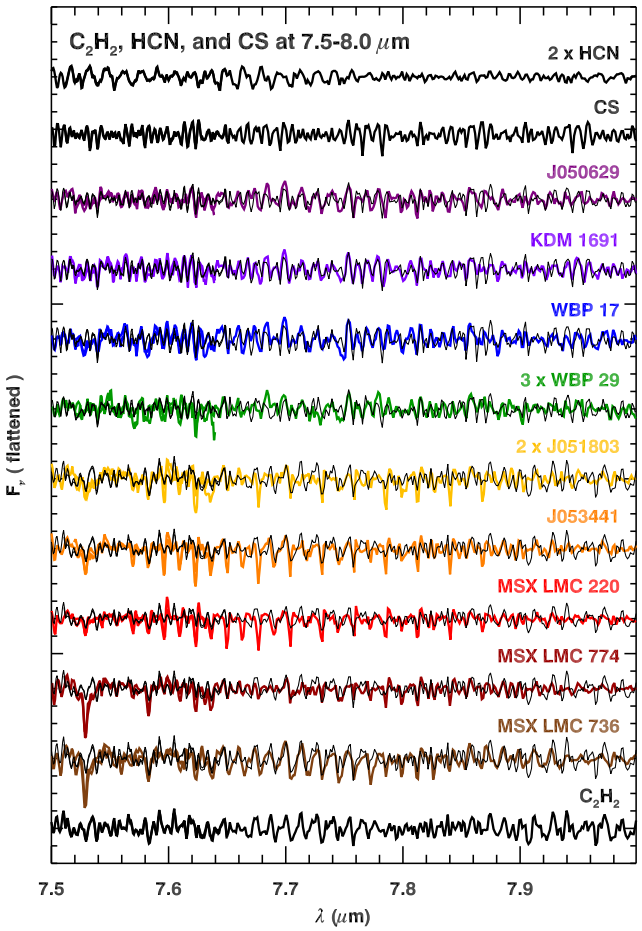

Figure 21. As Figure 20, except for 7.5–8.0 μm.

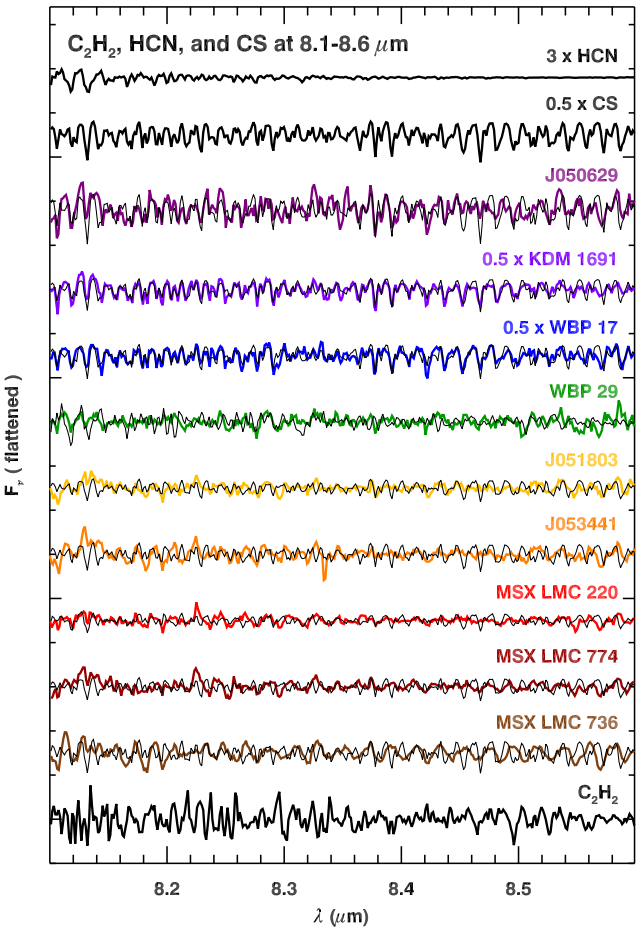

Figure 22. As Figure 20, but for the interval 8.1–8.6 μm.

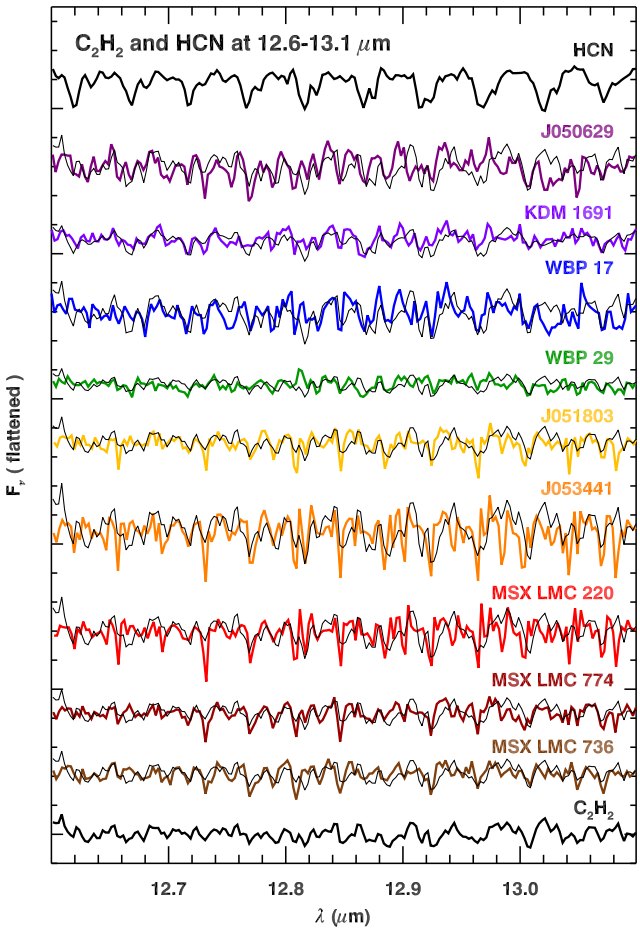

Figure 23. The flattened observed spectra at 12.6–13.1 μm (in color) compared to fitted molecular spectra (black). The HCN spectrum at the top is for $T_{\rm eff}$ = 3100 K and a C/O ratio = 2.0. The C_2H_2 at the bottom is for 2800 K and the same C/O ratio. The observed spectra are corrected for the radial velocities in Table 3. This figure will be part of Figure Set 18 in the published paper.

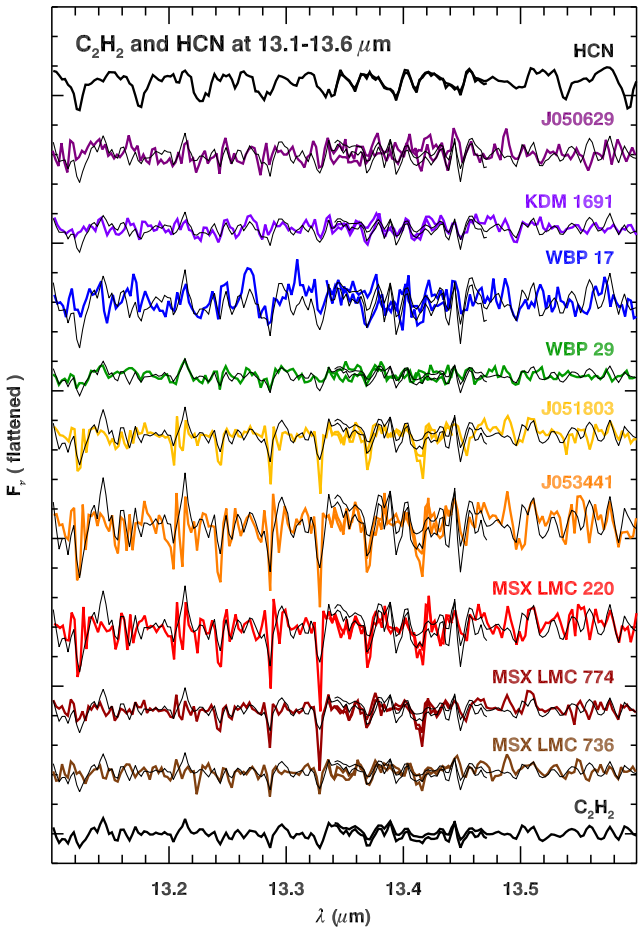

Figure 24. As Figure 23, but for 13.1–13.6 μm.

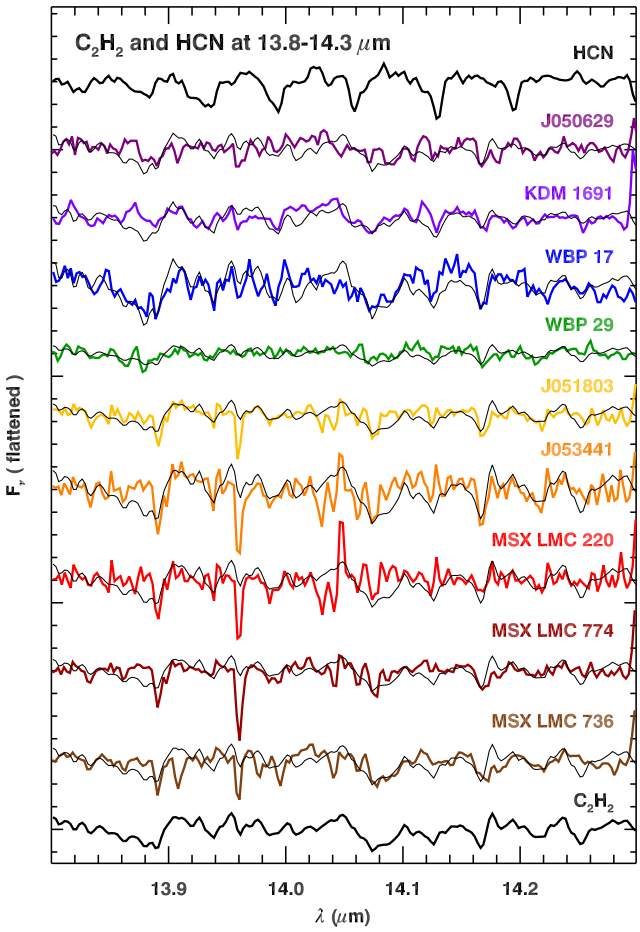

Figure 25. As Figure 23, but for 13.8–14.3 μm.

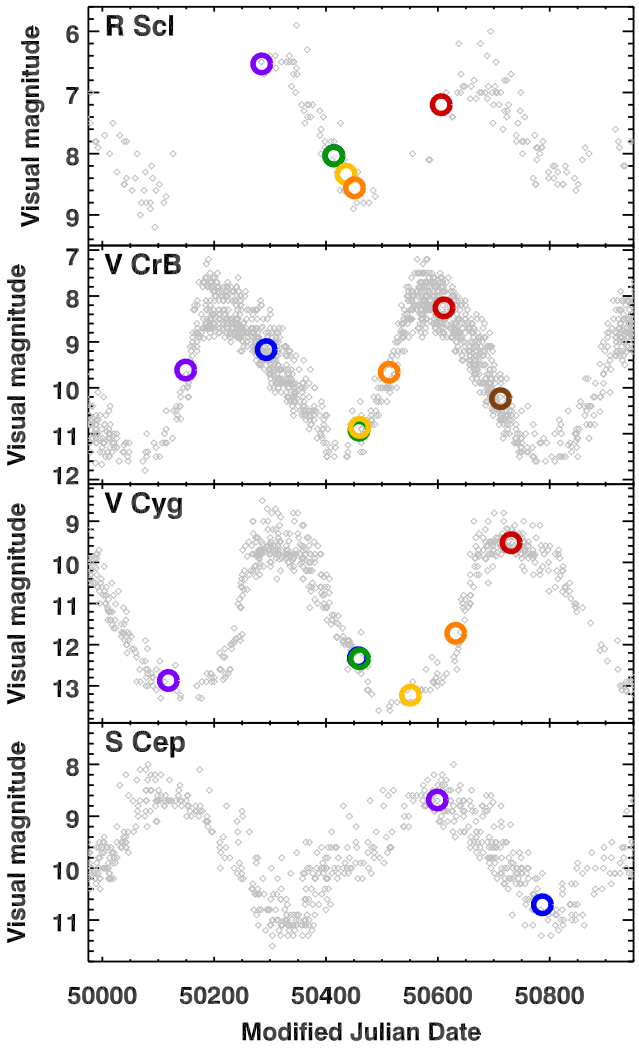

Figure 26. Light curves from the AAVSO in gray with the epochs of the SWS observations plotted in color. The magnitudes at the SWS epochs are estimated from AAVSO observations with ±20 days. In the panels for R Scl and V Cyg, the second and third spectra were obtained the same day, so the green plotting symbol completely covers the blue. Figure 27 plots the spectra in the same colors. In the published paper, this figure will be Figure 19.

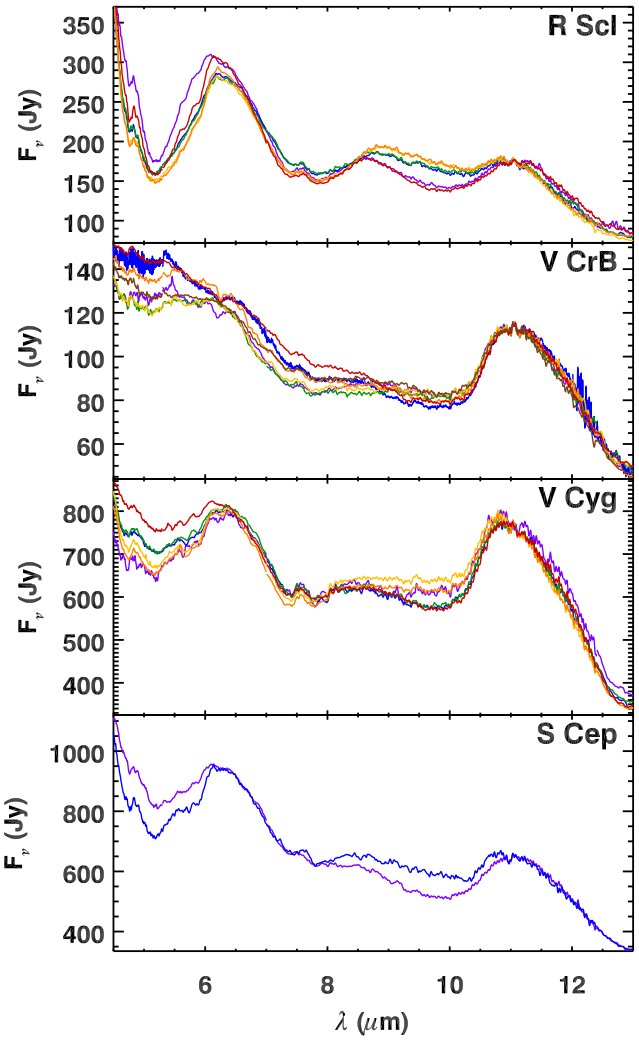

Figure 27. Spectra from each SWS observation for the four Galactic carbon stars chosen to compare the behavior of the 10 μm absorption band. The spectra are plotted with the same colors as Figure 26. All spectra are normalized to the first spectrum at 11.0–11.2 μm. In the published paper, this figure will be Figure 20.

REFERENCES

Allamandola, L. J., Tielens, A. G. G. M., & Barker, J. R. 1989, ApJS, 71, 733

Aoki, W., Tsuji, T., & Ohnaka, K. 1998, A&A, 340, 222

Aoki, W., Tsuji, T., & Ohnaka, K. 1999, A&A, 350, 945

Aringer, B., Girardi, L., Nowotny, W., et al. 2016, MNRAS, 457, 3611

Aringer, B., Marigo, P., Nowotny, W., et al. 2019, MNRAS, 487, 2133

Barber, R. J., Strange, J. K., Hill, C., et al. 2014, MNRAS, 437, 1828

Bernard-Salas, J., Peeters, E., Sloan, G. C., et al. 2009, ApJ, 699, 1541

Bladh, S., Eriksson, K., Marigo, P., et al. 2019, A&A, 623, L119

Blanco, B. M., Blanco, V. M., & McCarthy, M. F. 1978, Nature, 271, 638

Blanco, V. M., McCarthy, M. F., & Blanco, B. M. 1980, ApJ, 242, 938

Boyer, M. L., Sloan, G. C., Nanni, A., et al. 2025, ApJ, 991, 24

Boyer, M. L., Srinivasan, S., Riebel, D., et al. 2012, ApJ, 748, 40

Chiar, J. E., & Tielens, A. G. G. M. 2006, ApJ, 637, 774

Cherchneff, I. 2006, A&A, 456, 1001

Choudhury, S., Subramaniam, A., & Cole, A. A. 2016, MNRAS, 455, 1855

Chubb, K. L, Tennyson, J., & Yurchenko, S. N. 2020, MNRAS, 493, 1531

Cioni, M.-R. L., Clementini, G., Girardi, L., et al. 2011, A&A, 527, 116

Cioni, M.-R. L., & Habing, H. J. 2003, A&A, 402, 133

Cioni, M.-R. L., Loup, C., Habing, H. J., et al. A&AS, 114, 235

de Graauw, T., Haser, L. N., Beintema, D. A., et al. 1996, A&A, 315, L49

Dwek, E., Galliano, F., & Jones, A. P. 2007, ApJ, 662, 927

Eriksson, K., Höfner, S., & Aringer, B. 2023, A&A, 673, 21

Fazio, G. G., Hora, J. L., Allen, L. E., et al. 2004, ApJS, 154, 10

Fraser, O. J., Hawley, S. L, & Cook, K. H. 2008, AJ, 136, 1242

Fraser, O. J., Hawley, S. L, Cook, K. H., & Keller, S. C. 2005, AJ, 129, 768

Frenklach, M., & Feigelson, E. D. 1989, ApJ, 341, 372

Gaia Collaboration, Prusti, T., de Bruijne J. H. H., et al 2016, A&A, 595, 1

Gaia Collaboration, Brown, A. G. A., Vallenari, A., et al. 2021, A&A, 649, 1

Gaia Collaboration, Vallenari, A., Brown, A. G. A., et al. 2023, A&A, 674, 1

Gardner, J. P., Mather, J. C., Abbot, R., et al. 2023, PASP, 135, 68001

Gautschy-Loidl, R., Höfner, S., Jorgensen, U. G., & Hron, J. 2004, A&A, 422, 289

Groenewegen, M. A. T. 2004, A&A, 425, 595

Groenewegen, M. A. T. 2022, A&A, 659, 145

Groenewegen, M. A. T., Nanni, A., Cioni, M.-R. L., et al. 2020, A&A, 636, 48

Groenewegen, M. A. T., Sloan, G. C., Soszyński, I., & Petersen, E. A. 2009, A&A, 506, 1277

Groenewegen, M. A. T., & Sloan, G. C. 2018, A&A, 609, 114

Groenewegen, M. A. T., Wood, P. R., & Sloan, G. C. 2007, MNRAS, 376, 313

Habing, H. J. 1996, A&A Rv, 7, 97

Harris, G. J., Larner, F. C., Tennyson, J., et al. 2008, MNRAS, 390, 143

Helton, J. M., Morrison, J. E., Hainline, K. N., et al. 2026, ApJL, submitted (arXiv 2512.19695)

Herwig, F. 2004, ApJS, 155, 651

Höfner, S., Bladh, S., Aringer, B., & Ahuja, R. 2016, A&A, 594, 108

Höfner, S. & Olofsson, H. 2018, A&A Rv, 26, 1

Houck, J. R., Roellig, T. L., & van Cleve, J., et al. 2004, ApJS, 154, 18

Iben, I., & Renzini, A. 1983, ARA&A, 21, 271

Ita, Y., Tanabé, T., Matsunaga, N., et al. 2004, MNRAS, 353, 705

Iwanek, P., Soszyński, I., & Kozłowski, S. 2021, ApJ, 919, 99

Kato, D., Nagashima, C., Nagayama, T., et al. 2007, PASJ, 59, 615

Kessler, M., Anderegg, M. E., Clavel, J., et al. 1996, A&A, 315, L27

Kessler, M., Müller, T. G., Leech, K., et al. 2003, The ISO Handbook, Vol. I: ISO—Mission & Satellite Overview (ESA SP-1262)

Kim, D.-W., Protopapas, P., Bailer-Jones, C. A. L., et al. 2014, A&A, 566, 43

Kloppenborg, B. K. 2025, Observations from the AAVSO International Database (https://www.aavso.org)

Kraemer, K. E., Sloan, G. C., Keller, L. D., et al. 2019, ApJ, 887, 82

Lallement, R., Vergely, J. L., Babusiaux, C., & Cos, N. L. J. 2022, A&A, 661, 147

Law, D. R., Argyriou, I., Gordon, K. D., et al. 2024, AJ, in press (arXiv 2409.15435)

Leech, K., Kester, D., Shipman, R., et al. 2003, The ISO Handbook, Vol. V: SWS—The Short Wavelength Spectrometer (ESA SP-1262)
Leisenring, J., Kemper, F., & Sloan, G. C. 2008, ApJ, 681, 1557
Li, G., Gordon, I. E., Rothman, L. S., et al. 2015, ApJS, 216, 15
Liljegren, S., Höfner, S., Nowotny, W., & Eriksson, K. 2016, A&A, 589, 130
Loidl, R., Hron J., HöFner, S., et al. 1997, Ap&SS, 251, 243
Lynas-Gray, A. E., Polyansky, L., Tennyson, J., et al. 2024, MNRAS, 535, 1439
Mainzer, A., Bauer, J., Cutri, R. M., et al. 2014, ApJ, 792, 30
Maiolino, R., Schneider, R., Oliva, E., et al. 2004, Nature, 431, 533
Martin, P. G., & Rogers, C. 1987, ApJ, 322, 374
Matsuura, M., Barlow, M. J., Zijlstra, A. A. et al. 2009, MNRAS, 396, 918
Matsuura, M., Wood, P. R., Sloan, G. C., et al. 2006, MNRAS, 371, 415
Matsuura, M., Woods, P. M., & Owen, P. J. 2013, MNRAS, 429, 2527
Mattsson, L., Wahlin, R., Höfner, S., et al. 2008, A&A, 484, L5
Mattsson, L., Wahlin, R., & Höfner, S. 2010, A&A, 509, 14
McDonald, I., Srinivasan, S., Scicluna, P., et al. 2025, MNRAS, 541, 516
McDonald, I., & Trabuchhi, M. 2019, MNRAS, 484, 4678
McDonald, I., Zijlstra, A. A., Cox, N. L. J., et al. 2024, RASTI, 3, 89
Meixner, M., Gordon, K. D., Indebetouw, R., et al. 2006, AJ, 132, 2268
Naidu, R. P., Oesch, P. A., Brammer, G., et al. 2026, OJAp, in press (arXiv 2505.11263)
Onken, C. A., Wolf, C., Bessell, M. S., et al. 2024, PASA, 41, 61
Ou, J.-Y., & Ngeow, C.-C. 2022, AJ, 163, 192
Ochsenbein, F., et al. 2000, "The VizieR database of astronomical catalogues," DOI: 10.26093/cds/vizier
Paulose, G., Barton, E. J., Yurchenko, S. N., & Tennyson, J. 2015, MNRAS, 454, 1931
Piatti, A. E., & Geisler, D. 2013, AJ, 145, 17
Pietrzyński, G., Graczyk, D., Gallenne , A., et al. 2019, Nature, 567, 200
Pontoppidan, K. M., Salyk, C., Banzatti, A., et al. 2024, ApJ, 963, 158
Renzini, A., & Voli, M. 1981, A&A, 94, 175
Riebel, D., Boyer, M. L., Srinivasan, S., et al. 2015, ApJ, 807, 1
Rieke, G. H., & Lebofsky, M. H. 1985, ApJ, 288, 618
Salpeter, E. E. 1952, ApJ, 115, 326
Samus, N. N., Kazarovets, E. V., Durlevich, O. V., et al. 2017, ARep, 61, 1
Sanford, R. F. 1944, ApJ, 99, 145
Siderud, E., Eriksson, K., Höfner, S., & Bladh, S. 2025, A&A, 697, 52
Skrutskie, M. F., Cutri, R. M., Stiening, R., et al. 2006, AJ, 131, 1163
Sloan, G. C., Kraemer, K. E., Aringer, B., et al. 2024, Galaxies, 12, 61
Sloan, G. C., Kraemer, K. E., Price, S. D., & Shipman, R. F. 2003, ApJS, 147, 379
Sloan, G. C., Kraemer, K. E., Wood, P. R., et al. 2008, ApJ, 686, 1056
Sloan, G. C., Kraemer, K. E., McDonald, I., et al. 2016, ApJ, 826, 44
Sloan, G. C., Lagadec, E., Kraemer, K. E., et al. 2015, in *Why Galaxies Care about AGB Stars III*, ed. F. Kerschbaum, J. Hron, & R. Wing, ASP Conf. Series, 497, 429
Sloan, G. C., Matsuura, M., Lagadec, E., et al. 2012, ApJ, 752, 140
Soszyński, I., Udalski, A., Szymański, M. K., et al. 2009, AcA, 59, 335
Spano, M., Mowlavi, N., Eyer, L., et al. 2011, A&A, 536, 60
Srinivasan, S., Boyer, M. L., Kemper, F., et al. 2016, MNRAS, 457, 2814
Straniero, O., Abia, C., Domińguez, I. 2023, EPJA, 59, 17
Todini, P., & Ferrara, A. 2001, MNRAS, 325, 726
Vassiliadis, E., & Wood, P. R. 1993, ApJ, 413, 641
Wells, M., Pel, J.-W., Glasse, A., et al. 2015, PASP, 127, 646
Werner, M. W., Roellig, T. L., Low, F. J., et al. 2004, ApJS, 154, 1
Whitelock, P. A., Menzies, J. W., Feast, M. W., et al. 2009, MNRAS, 394, 795
Wickramasinghe, N. C., Donn, B. D., & Stecher, T. P. 1966, ApJ, 146, 590
Woitke, P. 2006, A&A, 452, 537
Wright, E. L., Eisenhardt, P. R. M., Mainzer, A. K., et al. 2010, AJ, 140, 1868
Wright, G. S., Rieke, G. H., Glasse, A., et al. 2023, PASP, 135, 048003
Yamashita, Y. 1975, AnTok, 15, 47
Zaritsky, D., Harris, J., Thompson, I. B., & Grebel, E. K. 2004, AJ, 128, 1606